Wave Motion 142 (2026) 103704

Contents lists available at ScienceDirect

Wave Motion

journal homepage: www.elsevier.com/locate/wamot

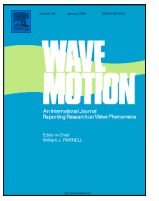

# Analysis of sound radiation from a vibrating clamped thin rectangular plate without baffle and in the rigid baffle using exact formulas

Wojciech P. Rdzanek [a,*], Jerzy Wiciak [b], Krzysztof Szemela [a], Marek Pawelczyk [c], Li Cheng [d]

[a] Faculty of Exact and Technical Sciences, Institute of Physics, University of Rzeszow, Prof. S. Pigonia 1, 35-310, Rzeszow, Poland
[b] Faculty of Mechanical Engineering and Robotics, Department of Mechanics and Vibroacoustics, AGH University of Science and Technology, Al. Mickiewicza 30 30-059 Kraków, Poland
[c] Department of Measurements and Control Systems, Silesian University of Technology, Akademicka 16, 44-100, Gliwice, Poland
[d] Department of Mechanical Engineering, The Hong Kong Polytechnic University, Hong Kong, China

ARTICLE INFO

Dr W Parnell

*Keywords:*
Boundary value problem
Rectangular plate
Acoustic field
Air-structure interactions
Acoustic impedance
No baffle

ABSTRACT

This study presents an analysis of sound radiation from a vibrating thin clamped rectangular plate using exact formulas. A new analytical approach–referred to here as the *theoretical approximate formulas method*–is proposed and applied to cases where the plate is either embedded in a rigid infinite baffle or has no baffle at all. The exact eigenfrequencies of the plate are obtained from a system of five coupled characteristic equations, as reported in the literature. The biharmonic equation governing the plate's vibrations is coupled with the Helmholtz equation on both sides of the plate, thereby incorporating acoustic attenuation into the model. To represent the acoustic pressure and radiated acoustic power, a double Fourier transform is employed. These quantities are expressed as expansion series involving double infinite integrals. The integrals are evaluated exactly using the spectral mapping method, the Dini series, and radial polynomials.

The resulting solutions are accurate and rapidly convergent, spanning from frequencies below the plate's fundamental frequency to those above its critical frequency. Consequently, the proposed method enables effective and precise solutions to both Neumann and Dirichlet boundary value problems, and facilitates detailed analysis of the resulting acoustic fields. The findings can be applied to predict the acoustic behavior of structural casing elements shaped in the form of thin rectangular plates, in industrial environments. Selected numerical examples are also provided to demonstrate the method's applicability.

## 1. Introduction

Thin plates are often used in industry as cover plates and as components of casings of various machines. Such plates are subject to excited vibration and, consequently, radiate acoustic waves. Therefore, the sound radiation from thin vibrating rectangular plates has attracted considerable attention from many researchers. The acoustic field generated is analyzed using different methods, such as variational methods, the finite element method (FEM), and experimental approaches. Analyses using exact formulas are relatively rare and usually restricted to specific cases.

* Corresponding author.
*E-mail address:* wprdzank@ur.edu.pl (W.P. Rdzanek).

https://doi.org/10.1016/j.wavemoti.2026.103704
Received 11 January 2025; Received in revised form 29 September 2025; Accepted 15 January 2026
Available online 17 January 2026

Leppington et al. [1] analytically investigated the acoustic radiation efficiency of simply supported rectangular panels. Berry et al. [2] derived general expressions for sound radiation from rectangular baffled plates with arbitrary boundary conditions. They applied the approximate Rayleigh–Ritz method to solve the equations of motion and performed analytical calculations to determine the radiation efficiency. Atalla et al. [3] used the Rayleigh-Ritz approximation for the eigenfrequencies and mode shapes of a rectangular plate with general boundary conditions. They then presented formulas for the acoustic field of the unbaffled plate. In numerical analysis, they focused on the influence of the specific boundary conditions of the plate on the radiation efficiency. They considered simply supported and free edges of the plate, conducted limited comparative analyses between the sound radiation of baffled and unbaffled plates, and carried out limited experimental studies of the acoustic field. Sung and Jan [4] obtained approximate eigenfrequencies of a clamped rectangular plate and presented the radiated acoustic power. They derived approximate solutions for the vibration problem of the plate based on the virtual work principle. Two concentrated forces were applied to emulate a single excitation moment on the plate. The acoustic power was calculated using the double Fourier transform. Their experimental results were slightly smaller than the theoretical values, probably due to diffraction at the edges of the finite baffle, in contrast to the infinite baffle assumed in theoretical calculations, which is especially important at the low-frequency limit. Laulagnet [5] presented a rigorous analysis of the sound radiation of a vibrating simply supported rectangular plate with no baffle (WNB). He solved the coupled system of the biharmonic equation and the Helmholtz equation by applying the modal expansion of the vibration velocity of the plate and the two-dimensional Fourier transform for calculating the modal impedance coefficients. Li and Gibeling [6] analyzed the effect of including the self- and mutual radiation resistances of a simply supported rectangular plate in rigorous calculations of the radiated sound power. They illustrated the influence of including or neglecting the mutual radiation resistances on the calculated total acoustic power. Li [7] presented further efficient analytical solutions for the real component of the self- and mutual radiation resistances of a simply supported rectangular plate in the form of double surface integrals. Hashimoto [8] proposed a practical measurement method for the radiation efficiency of a vibrating thin clamped panel, referred to as the discrete calculation method. This method is based on measuring the normal vibration velocity on the plate discretized into elements small compared to the wavelength. The acoustic field was then calculated as the superposition of the fields radiated by the elements considered as circular pistons. This method is equivalent to numerical integration of the Rayleigh first integral, while integrating the field over the surface of the plate yields the acoustic power. In this method, the ratio of the discretized element size to the wavelength corresponds to the approximation error: the greater the ratio, the larger the error.

Arenas and Crocker [9] analyzed the radiation efficiency of baffled clamped and simply supported rectangular plates excited by point forces. They used the resistance matrix method proposed earlier by Hashimoto. Zawieska et al. [10,11] presented the low-frequency approximation for the modal self- and mutual impedance coefficients of a vibrating simply supported rectangular plate. Currey and Cunefare [12] presented theoretical expressions for the radiation resistances of simply supported plates. They expressed the sound power radiated from a plate in terms of the normal velocity distribution on the plate and a coupling matrix. Their velocity distribution on the plate was expressed in terms of the modal amplitudes and normal modes. Zou and Crocker [13] analyzed the sound power radiated from rectangular plates for six different boundary configurations of the plate edges. They applied the method presented earlier by Currey and Cunefare, with the key issue being to find the coupling matrix for the boundary conditions of interest. Putra and Thompson [14] analyzed the sound radiation efficiency of a vibrating thin rectangular plate with pairs of edges either simply supported or guided. They used approximate eigenfrequencies and eigenvalues (proposed earlier by Warburton [15]), and included only the modal mutual impedance coefficients in their numerical calculations, obtaining results up to frequencies above the critical frequency of the plates. Kolber et al. [16] applied the DCM to examine the effect of plate discretization on the accuracy of sound radiation efficiency measurements. This method is essentially equivalent to the method presented earlier by Hashimoto. Mellow and Kärkkäinen [17] presented a rigorous analysis of the radiation impedance of a rectangular piston vibrating in an infinite rigid baffle. They obtained some highly convergent expansion series useful at low frequencies. Hasheminejad and Keshavarzpour [18] proposed an algorithm for an active sound radiation control system for a thick piezolaminated smart rectangular plate, based on a semi-analytic solution for the coupled vibroacoustic response of a simply supported, arbitrarily thick, piezolaminated rectangular plate embedded in an infinite rigid baffle. They applied the linear three-dimensional piezoelasticity theory in conjunction with the classical Rayleigh integral, while the responses of their smart plate were controlled by an integrated layer with spatially distributed piezoelectric sensors and actuators. It was shown numerically that the proposed control system was capable of suppressing the predicted sound radiation response of the plate. Hasheminejad et al. [19] presented a similar algorithm for suppressing the vibroacoustic responses of a rectangular point-excited, simply supported, sandwich electrorheological panel. Pawelczyk and Wrona [20] presented several practical applications of the rigorous analysis of sound radiation of vibrating thin rectangular plates as elements of machine casings in industrial environments. Dikshit and Sonti analytically studied sound transmission of an obliquely incident plane wave passing through an unbaffled simply supported plate using the double Fourier transform method [21]. Dikshit et al. presented a closed-form expression for the resonance frequencies of an unbaffled simply supported rectangular water-loaded plate [22]. As shown above, considerable work has been carried out on sound radiation of rectangular plates. Most studies, however, either employ the approximate Rayleigh-Ritz method to find the eigenfrequencies and eigenfunctions of the plates, or they focus on exact solutions for limited boundary configurations. In the case of the Rayleigh-Ritz method, the results are accurate only at the lowest frequencies. In the case of exact solutions, recent results are restricted to plates where both the eigenfrequencies and eigenfunctions assume simple forms, including plates simply supported on all edges or plates with two opposite edges simply supported and the other two guided. Dealing with more complex boundary configurations leads to complex algorithms, such as those applied by Zou and Crocker [13]. The main limitation of the exact solutions presented so far is that the plate edges are either simply supported, clamped, or mixed configurations such as SS-C-SS-C or SS-F-SS-F (here SS stands for a simply supported edge, C for a clamped edge, and F for a free edge). However, these boundary configurations are of limited practical use for cases such as a glass plate in a rectangular window, where all the edges have similar or identical boundary

conditions. Although it is uncertain whether the edges of such glass plates are clamped or simply supported, they are unlikely to match mixed configurations such as SS-C-SS-C or SS-F-SS-F. Therefore, addressing the case of the C-C-C-C plate could represent significant progress. On the other hand, the approximate eigenfrequencies and eigenfunctions obtained using methods such as the Rayleigh-Ritz approach result in error propagation when calculating radiation impedances and subsequently solving systems of equations. Hence, they are reliable only for the lowest frequencies. Therefore, applying exact solutions of the eigenvalue problem for free vibrations of the C-C-C-C plate is of utmost importance, as only negligible numerical errors would be propagated from this stage to the radiation impedances and the solution of systems of equations. If, in addition, the radiation impedance could be calculated exactly, even smaller numerical errors would propagate to the subsequent systems of equations. The main aim of this study is to address this problem and provide the theoretical approximate formulas method (TAFM) for the sound radiation of a thin rectangular plate clamped along its entire circumference, considering two major cases: the plate WNB and the plate embedded in a rigid infinite baffle (RIB). In this case, the system of coupled characteristic equations, presented recently by Xing and Liu [23], must be applied. This leads to exact solutions for free vibrations of thin rectangular clamped plates. For this purpose, they used their symplectic dual method. Solving their system of characteristic equations yields the exact eigenvalues and eigenfunctions of clamped plates. In this study, this exact approach to the eigenvalue problem has been applied. Further, the Fourier transforms of the eigenfunctions of the plate have been presented in a form suitable for obtaining the acoustic pressure and acoustic power of the vibrating plate, expressed as a double inverse Fourier transform useful for numerical calculations (i.e., the transforms are rearranged using the boundary conditions of the plate in such a way that the hyperbolic functions are eliminated). The resulting double integrals for the modal admittance coefficients exhibit troublesome singularities and, overall, the calculations are time-consuming. Therefore, the double integrals have been transformed using the relation between the double inverse Fourier transforms and series of single inverse Hankel transforms, as mentioned by Cornacchio and Soni [24] and Baddour [25]. The latter contain only single integrals, which simplifies further numerical analysis. However, this results in expansion coefficients expressed in the form of double integrals. These coefficients have been presented here as rapidly convergent expansion series, independent of frequency and therefore calculable a priori, i.e., before any calculations of the acoustic field are performed. The obtained single inverse Hankel transform has been spectrally mapped to a set of integrals that can be expressed in terms of generalized hypergeometric functions, which are readily available in Python and similar programming languages (cf. e.g. Rdzanek and Szemela [26]). For this purpose, the formalism of radial polynomials (connected with the circular Zernike polynomials widely used in optics) has been applied. It is important to note that although the spectral mapping method has previously been successfully applied to problems of sound radiation by vibrating circular and annular plates and apertures, it is not obvious that this method would also be applicable to rectangular plates while still providing exact and numerically accurate results. Nevertheless, this was achieved by employing the aforementioned relation between the double inverse Fourier transforms and series of single inverse Hankel transforms. Finally, all formulas are theoretically exact and numerically accurate, except for numerical errors due to truncation, which are then propagated when solving the system of algebraic equations. By numerically accurate, it should be understood here as achievable with arbitrary numerical precision.

The TAFM presented in this study can be applied for rapid and accurate calculations of acoustic power, radiation efficiency, and acoustic pressure of thin clamped rectangular plates, whether in the RIB or WNB. The numerical results are valid across a wide frequency range, from below the fundamental frequencies of the plates to frequencies far exceeding their critical values.

Such high accuracy has been achieved by determining the exact eigenvalues and eigenfunctions of the clamped plate. In addition, the radiation impedances and admittances have also been calculated exactly. This was accomplished using the spectral mapping method and reducing the formulas for the modal self-impedance and mutual coefficients of the plate in the RIB from their double inverse Fourier transform form into rapidly converging expansion series. These coefficients can subsequently be used to calculate, relatively rapidly, the modal admittance coefficients of the WNB plate. Consequently, the coefficients can be determined efficiently and accurately, regardless of frequency. A secondary aim is to present sample numerical results, to examine the frequency limits within which the formulas provide reliable outcomes, and to validate the numerical results using other methods such as FEM. Potential practical applications of TAFM include theoretical predictions of the acoustic field and acoustic power of various industrial systems containing thin clamped rectangular plates, whenever they can be treated as plates in infinite baffles or when the effect of the baffle is negligible. This method can also be used to obtain reference values to validate results produced by different approximate methods, including FEM. This study is organized as follows. Section 2.1 presents the statement of the problem. Section 2.2 presents the free vibrations, characteristic equations, and eigenfunctions of a thin rectangular plate clamped on all its edges. Section 2.3 presents the Fourier transforms of the eigenfunctions of the plate. Section 2.4 presents the solutions for the sound radiation of the excited vibrations of the WNB plate. Section 2.5 presents the solutions for the sound radiation of the excited vibrations of the plate in the RIB. Section 3 describes the spectral mapping method for obtaining modal admittance coefficients in the form of rapidly converging expansion series useful for numerical calculations. Section 4 presents the numerical analysis. In Section 5, the conclusions are drawn. Some detailed mathematical derivations are presented in Appendix A–E.

## 2. The governing equations

### 2.1. Statement of the problem

The problem of sound radiation from a thin rectangular plate clamped on all its edges is considered. The plate is either embedded in the RIB or in the WNB. In the first case, the Neumann boundary condition, corresponding to zero normal particle velocity (i.e., a rigid boundary), is satisfied throughout the plane of the plate — both on the plate itself and in the surrounding medium. In the second case, the Neumann condition is enforced only on the plate, whereas in the region outside the plate, the Dirichlet boundary

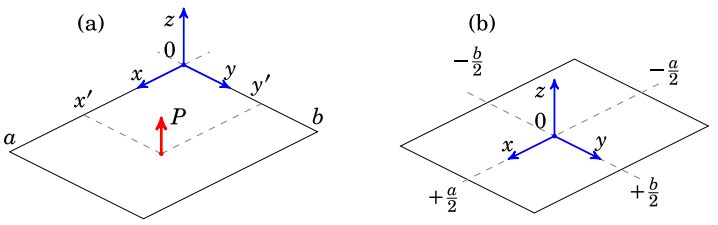


**Fig. 1.** Geometry of the clamped rectangular plate of dimensions $a \times b \times h$ in rectangular coordinates $(x, y)$, where $(x', y')$ are the coordinates of the point where the concentrated force is applied to the plate, suitable for: (a) the vibration problem, (b) the radiation problem.

condition (corresponding to zero acoustic pressure) is imposed. In this second scenario, the acoustic pressure is continuous across the plate plane except at the location of the plate itself, where a discontinuity occurs.

The plate is excited by a time-harmonic concentrated external force. The problem is solved exactly.

### 2.2. The free vibrations of the plate

The exact solutions for the eigenfrequencies and eigenfunctions of a thin clamped rectangular plate were presented earlier by Xing and Liu [23]. Therefore, only the necessary equations are summarized here for convenience.

A thin rectangular plate of dimensions $a \times b \times h$ with clamped edges is oscillating freely. The origin of the coordinates is located at the corner of the plate, i.e., at $x, y = 0$ (cf. Fig. 1(a)). Thus, the following biharmonic equation is satisfied (cf. Pierce [27] Eq. (1-6.1), Blackstock [28] Eq. (A.1) p. 2, and Meirovitch [29] Eq. (5.258))

$$\nabla^4 W_n(x, y) - k_n^4 W_n(x, y) = 0, \tag{1}$$

for $0 \leqslant x \leqslant a$ and $0 \leqslant y \leqslant b$, where $k_n = (\rho h \omega_n^2 / D_E)^{1/4}$ is the bending wavenumber, $D_E = Eh^3/[12(1-\nu^2)]$ is the bending stiffness, $h$ is the thickness of the plate ($h \ll a, b$), $W_n$ is the $n$th eigenfunction, $\omega_n$ is the $n$th angular eigenfrequency, $n = 1, 2, \ldots$, $n$ is the modal number in the order of increasing $k_n$ ($k_1 < k_2 \ldots$), each value of $n$ is associated with the unique pair of the modal numbers $q$ and $p$ such that $q$+1 and $p$+1 are the numbers of the nodal lines of the $n$th eigenfunction in the $x$ and $y$ directions (including the nodal lines at the edges of the plate), and $q, p = 1, 2, \ldots$. Consequently, $n \equiv (q, p)$. The time dependence is $\exp(-\mathrm{i}\omega t)$, where $\omega$ is the angular frequency and $t$ is time. The time dependence is suppressed throughout this study. The biharmonic and Laplace operators in rectangular coordinates assume, respectively, the forms of (cf. Rao [30] p. 487)

$$\nabla^4 = \nabla^2 \nabla^2, \qquad \nabla^2 = \frac{\partial^2}{\partial x^2} + \frac{\partial^2}{\partial y^2}. \tag{2}$$

The eigenfunction of the plate is given by (cf. Xing and Liu [23] Eqs. (13)–(20))

$$W_n(x, y) = \Psi_q(x) \Phi_p(y), \tag{3a}$$

$$\Psi_q(x) = A_{1,q} \left[ \cos(\alpha_{1,q} x) - \cosh(\alpha_{2,q} x) - \bar{k}_{1,q} \left( \frac{\alpha_{2,q}}{\alpha_{1,q}} \sin(\alpha_{1,q} x) - \sinh(\alpha_{2,q} x) \right) \right], \tag{3b}$$

$$\Phi_p(y) = A_{2,p} \left[ \cos(\beta_{1,p} y) - \cosh(\beta_{2,p} y) - \bar{k}_{2,p} \left( \frac{\beta_{2,p}}{\beta_{1,p}} \sin(\beta_{1,p} y) - \sinh(\beta_{2,p} y) \right) \right], \tag{3c}$$

where $\alpha_{1,q}$, $\alpha_{2,q}$, $\beta_{1,p}$, and $\beta_{2,p}$ are the characteristic values, and

$$\bar{k}_{1,q} = \frac{\cos(\alpha_{1,q} a) - \cosh(\alpha_{2,q} a)}{(\alpha_{2,q}/\alpha_{1,q}) \sin(\alpha_{1,q} a) - \sinh(\alpha_{2,q} a)} = \frac{-(\alpha_{1,q}/\alpha_{2,q}) \sin(\alpha_{1,q} a) - \sinh(\alpha_{2,q} a)}{\cos(\alpha_{1,q} a) - \cosh(\alpha_{2,q} a)}, \tag{4a}$$

$$\bar{k}_{2,p} = \frac{\cos(\beta_{1,p} b) - \cosh(\beta_{2,p} b)}{(\beta_{2,p}/\beta_{1,p}) \sin(\beta_{1,p} b) - \sinh(\beta_{2,p} b)} = \frac{-(\beta_{1,p}/\beta_{2,p}) \sin(\beta_{1,p} b) - \sinh(\beta_{2,p} b)}{\cos(\beta_{1,p} b) - \cosh(\beta_{2,p} b)}. \tag{4b}$$

The following boundary conditions are satisfied

$$W_n(0, y) = 0, \quad W_n(a, y) = 0; \quad 0 \leqslant y \leqslant b, \tag{5a}$$

$$W_n(x, 0) = 0, \quad W_n(x, b) = 0; \quad 0 \leqslant x \leqslant a, \tag{5b}$$

$$\frac{\partial}{\partial x} W_n(x, y)\Big|_{x=0} = 0, \quad \frac{\partial}{\partial x} W_n(x, y)\Big|_{x=a} = 0; \quad 0 \leqslant y \leqslant b, \tag{5c}$$

$$\frac{\partial}{\partial y} W_n(x, y)\Big|_{y=0} = 0, \quad \frac{\partial}{\partial y} W_n(x, y)\Big|_{y=b} = 0; \quad 0 \leqslant x \leqslant a. \tag{5d}$$

The system of the characteristic equations of the plate are

$$(\alpha_{2,q}^2-\alpha_{1,q}^2)\sin(\alpha_{1,q}a)\sinh(\alpha_{2,q}a)-2\alpha_{1,q}\alpha_{2,q}\Big[\cos(\alpha_{1,q}a)\cosh(\alpha_{2,q}a)-1\Big]=0, \tag{6a}$$

$$(\beta_{2,p}^2-\beta_{1,p}^2)\sin(\beta_{1,p}b)\sinh(\beta_{2,p}b)-2\beta_{1,p}\beta_{2,p}\Big[\cos(\beta_{1,p}b)\cosh(\beta_{2,p}b)-1\Big]=0, \tag{6b}$$

where $\alpha_{2,q}^2-\alpha_{1,q}^2=2\beta_{1,p}^2$, $\beta_{2,p}^2-\beta_{1,p}^2=2\alpha_{1,q}^2$, and the bending wavenumber $k_n$ on the plate can be obtained from $k_n^2=\alpha_{1,q}^2+\beta_{1,p}^2$ (cf. the text after Eq. (1)).

### 2.3. The Fourier transforms

The double forward and backward Fourier transforms of the eigenfunctions and their spectral densities are important in the further analysis of the acoustic field generated by the vibrating plate and can be presented as follows:

$$\bar{W}_n(k_x,k_y)=\bar{\Psi}_q(k_x)\bar{\Phi}_p(k_y), \tag{7a}$$

$$W_n(x+a/2,y+b/2)=\Psi_q(x+a/2)\Phi_p(y+b/2), \tag{7b}$$

where

$$\bar{\Psi}_q(k_x)=\frac{1}{\sqrt{2\pi}}\int_{-a/2}^{+a/2}\Psi_q(x+a/2)\mathrm{e}^{-\mathrm{i}k_x x}\mathrm{d}x, \tag{8a}$$

$$\bar{\Phi}_p(k_y)=\frac{1}{\sqrt{2\pi}}\int_{-b/2}^{+b/2}\Phi_p(y+b/2)\mathrm{e}^{-\mathrm{i}k_y y}\mathrm{d}y, \tag{8b}$$

$$\Psi_q(x+a/2)=\frac{1}{\sqrt{2\pi}}\int_{-\infty}^{+\infty}\bar{\Psi}_q(k_x)\mathrm{e}^{+\mathrm{i}k_x x}\mathrm{d}k_x, \tag{8c}$$

$$\Phi_p(y+b/2)=\frac{1}{\sqrt{2\pi}}\int_{-\infty}^{+\infty}\bar{\Phi}_p(k_y)\mathrm{e}^{+\mathrm{i}k_y y}\mathrm{d}k_y, \tag{8d}$$

and the origin of the coordinates has been shifted to the center of the plate (cf. Fig. 1(b)). It is important to note that the integration limits with respect to the spatial variables $x$ and $y$ are restricted to the intervals $(-a/2,+a/2)$ and $(-b/2,+b/2)$, respectively. This limit reflects the applied boundary conditions: either the normal component of the vibration velocity vanishes outside the plate in its plane, corresponding to a Neumann boundary condition, or the acoustic pressure is assumed to be zero beyond the physical boundaries of the plate, indicating a Dirichlet boundary condition. Further, the integrals in Eqs. (8a) and (8b) can be rearranged as follows

$$\bar{\Psi}_q(k_x)=\frac{A_{1,q}(2/\pi)^{1/2}k_n^2}{(k_x^2-\alpha_{1,q}^2)(k_x^2+\alpha_{2,q}^2)}\left\{\Big[\alpha_{1,q}g_{1,q}(0)-\mathrm{i}k_x f_{1,q}(0)\Big]\mathrm{e}^{+\mathrm{i}k_x a/2}-\Big[\alpha_{1,q}g_{1,q}(a)-\mathrm{i}k_x f_{1,q}(a)\Big]\mathrm{e}^{-\mathrm{i}k_x a/2}\right\}, \tag{9a}$$

$$\bar{\Phi}_p(k_y)=\frac{A_{2,p}(2/\pi)^{1/2}k_n^2}{(k_y^2-\beta_{1,p}^2)(k_y^2+\beta_{2,p}^2)}\left\{\Big[\beta_{1,p}g_{2,p}(0)-\mathrm{i}k_y f_{2,p}(0)\Big]\mathrm{e}^{+\mathrm{i}k_y b/2}-\Big[\beta_{1,p}g_{2,p}(b)-\mathrm{i}k_y f_{2,p}(b)\Big]\mathrm{e}^{-\mathrm{i}k_y b/2}\right\}, \tag{9b}$$

since $\alpha_{1,q}^2+\alpha_{2,q}^2=\beta_{1,p}^2+\beta_{2,p}^2=2k_n^2$, where

$$f_{1,q}(x)=\cos(\alpha_{1,q}x)-\bar{k}_{1,q}\frac{\alpha_{2,q}}{\alpha_{1,q}}\sin(\alpha_{1,q}x), \tag{10a}$$

$$f_{2,p}(y)=\cos(\beta_{1,p}y)-\bar{k}_{2,p}\frac{\beta_{2,p}}{\beta_{1,p}}\sin(\beta_{1,p}y), \tag{10b}$$

$$g_{1,q}(x)=\sin(\alpha_{1,q}x)+\bar{k}_{1,q}\frac{\alpha_{2,q}}{\alpha_{1,q}}\cos(\alpha_{1,q}x), \tag{10c}$$

$$g_{2,p}(y)=\sin(\beta_{1,p}y)+\bar{k}_{2,p}\frac{\beta_{2,p}}{\beta_{1,p}}\cos(\beta_{1,p}y). \tag{10d}$$

The orthogonality relation is (cf. Meirovitch [29] Sec. '5-5 Generalized Orthogonality. Expansion Theorem' pp. 140–143)

$$\frac{1}{ab}\int_0^a\int_0^b W_n(x,y)W_{n'}(x,y)\mathrm{d}y\mathrm{d}x=\delta_{nn'}. \tag{11}$$

The normalization constants $A_{1,q}$ and $A_{2,p}$ can be obtained from the following arbitrary normalization conditions $\int_0^a\Psi_q^2(x)\mathrm{d}x=a$ and $\int_0^b\Phi_p^2(y)\mathrm{d}y=b$, giving, respectively,

$$A_{1,q}=\left\{1-\frac{1}{2}\left(1-\frac{\alpha_{2,q}^2}{\alpha_{1,q}^2}\right)\left[\bar{k}_{1,q}^2-\frac{1}{\alpha_{2,q}a}\left(\bar{k}_{1,q}-\frac{\alpha_{1,q}}{\alpha_{2,q}}f_{1,q}(a)g_{1,q}(a)\right)\right]\right\}^{-1/2}, \tag{12a}$$

$$A_{2,p} = \left\{ 1 - \frac{1}{2}\left(1 - \frac{\beta_{2,p}^2}{\beta_{1,p}^2}\right)\left[\bar{k}_{2,p}^2 - \frac{1}{\beta_{2,p} b}\left(\bar{k}_{2,p} - \frac{\beta_{1,p}}{\beta_{2,p}} f_{2,p}(b) g_{2,p}(b)\right)\right]\right\}^{-1/2}. \tag{12b}$$

Note, that the constants $A_{1,q}$ and $A_{2,p}$ must be calculated individually for each mode number $n = 1, 2, \ldots$.

### 2.4. The sound radiation of the excited vibrations of the plate WNB

The equation of motion of the excited plate can be given as

$$\omega^2 \varrho h (k_D^{-4} \nabla^4 - 1) W(x + a/2, y + b/2) + e_f p(x, y, 0) = P(x + a/2, y + b/2), \tag{13}$$

where $k_D$ is the bending wavenumber ($k_D^4 = \omega^2 \varrho h / D$), $D = D_E(1 + \mathrm{i}\eta)$ is the complex bending stiffness, $\eta$ is the dimensionless damping coefficient, $W(x + a/2, y + b/2)$ is the transverse displacement amplitude of the plate, $P(x + a/2, y + b/2)$ (Pa) is the external excitation applied to the plate, and $p(x, y, 0)$ is the acoustic pressure at the plate's upper surface. Here, $e_f$ indicates whether only the plate's upper side is air-loaded ($e_f = 1$) or both sides are air-loaded ($e_f = 2$). Such a simple configuration change is possible only when the half-space below the plate is the mirror image of the half-space above the plate (see e.g. Levine and Leppington [31], Eqs. (24) and (28), where the acoustic pressure is taken twice, and the explanation of the effective damping coefficient in Eq. (33)). It is worth noting that Eq. (13) contains two kinds of vibration attenuation of the plate. The first is material damping inside the plate, represented by the complex bending wavenumber $k_D$. The second is air damping, represented by the acoustic pressure $e_f p(x, y, 0)$ on the plate surface. The latter is particularly interesting as it can be obtained by solving the following Helmholtz equation

$$\left(\frac{\partial^2}{\partial x^2} + \frac{\partial^2}{\partial y^2} + \frac{\partial^2}{\partial z^2} + k_0^2\right) p(x, y, z) = 0, \tag{14}$$

where $k_0$ is the acoustic wavenumber $\omega = k_0 c$ is the driving circular frequency, and $c$ is the speed of sound. It is important to note that Eqs. (13) and (14) form a system of two coupled differential equations to be solved. After some mathematical manipulations, this system reduces to algebraic equations to be solved separately for each frequency sample. It is shown in this section how the system can be obtained. The vibrating plate satisfies the following Neumann boundary condition (cf. Fig. 1(b))

$$\left.\frac{\partial p}{\partial z}\right|_{z=0} = \mathrm{i}\omega \varrho_0 v(x + a/2, y + b/2), \tag{15}$$

on the plate for $-a/2 < x < +a/2$, $-b/2 < y < +b/2$, and $z = 0$, where the normal component of the vibration velocity on the plate is

$$v(x + a/2, y + b/2) = -\mathrm{i}\omega W(x + a/2, y + b/2), \tag{16}$$

and $W(x + a/2, y + b/2)$ is the transverse displacement amplitude of the plate presented in Eq. (3a).

The transverse displacement amplitude of the plate and the external excitation amplitude on the plate can be expressed as follows (cf. Fig. 1(a) and Eq. (13))

$$W(x, y) = \sum_{n=1}^{\infty} c_n W_n(x, y), \tag{17a}$$

$$P(x, y) = \sum_{n} \hat{P}_n W_n(x, y), \tag{17b}$$

for $0 \leqslant x \leqslant a$ and $0 \leqslant y \leqslant b$, where $c_n$ are unknown coefficients (to be obtained by solving the aforementioned system of algebraic equations). For $W_n(x, y)$ see Eq. (3a), and

$$\hat{P}_n = \frac{1}{ab} \int_0^a \int_0^b P(x, y) W_n(x, y) \mathrm{d}y \mathrm{d}x. \tag{18}$$

The most useful excitation is the point excitation. It can be formulated as

$$P(x, y) = P_0 ab\, \delta(x - x') \delta(y - y'), \tag{19}$$

where $P_0$ is the excitation amplitude, and $(x', y')$ are the rectangular coordinates of the excitation point on the plate. The modal excitation coefficients can be obtained by substituting the above equations into Eq. (18)

$$\hat{P}_n = P_0 W_n(x' + a/2, y' + a/2). \tag{20}$$

The acoustic pressure amplitude appearing in the system of two differential equations, Eqs. (13) and (14), can be expressed using the Kirchhoff-Helmholtz integral equation as follows (cf. Fahy and Gardonio [32], Eqs. (3.184)–(3.186), pp. 236–237, and also Atalla et al. [3], Eq. (6))

$$p(\vec{r}) \int_{S'} \left[\frac{\partial G(\vec{r}, \vec{r}\,')}{\partial n'} p(\vec{r}\,') - \frac{\partial p(\vec{r}\,')}{\partial n'} G(\vec{r}, \vec{r}\,')\right] \mathrm{d}S', \tag{21}$$

where $S'$ denotes the surface enclosing both sides of the plate, $\vec{n}'$ is the unit vector normal outward to the surface $S'$ of the plate, $\vec{n}' = +\vec{e}_z$ on the upper side of the plate and $\vec{n}' = -\vec{e}_z$ on the lower side, $\partial/\partial n' = \vec{n}' \cdot \nabla$ is the normal component of the gradient operator. The Green function for the entire free space in Eq. (21) is

$$G(\vec{r}, \vec{r}\,') = \frac{\mathrm{e}^{\mathrm{i}k_0 R}}{4\pi R} = \frac{\mathrm{i}}{8\pi^2} \int_{-\infty}^{+\infty} \int_{-\infty}^{+\infty} \mathrm{e}^{\mathrm{i}[k_x(x - x') + k_y(y - y') + k_z|z - z'|]} \frac{\mathrm{d}k_y \mathrm{d}k_x}{k_z}, \tag{22}$$

where $R = |\vec{R}| = [(x-x')^2 + (y-y')^2 + (z-z')^2]^{1/2}$, $\vec{R} = \vec{r} - \vec{r}\,'$, $\vec{r} = \vec{e}_x x + \vec{e}_y y + \vec{e}_z z$, and $\vec{r}\,' = \vec{e}_x x' + \vec{e}_y y' + \vec{e}_z z'$. This function satisfies the nonuniform wave equation

$$\nabla^2 G(\vec{r},\vec{r}\,') + k_0^2 G(\vec{r},\vec{r}\,') = \delta(\vec{r}-\vec{r}\,'), \tag{23}$$

where the Dirac delta is $\delta(\vec{r}-\vec{r}\,') = \delta(x-x')\delta(y-y')\delta(z-z')$. Note that the term with the normal pressure gradient on one side of the plate in Eq. (21) cancels this term on the other side of the plate, and only the term having the acoustic pressure remains and is doubled. This yields the acoustic pressure amplitude in the form of (for more details see Appendix B)

$$p(\vec{r}) = \int_{S'} 2p(x',y',0) \frac{\partial G(\vec{r},\vec{r}\,')}{\partial z'}\bigg|_{z'=0} \mathrm{d}S', \tag{24}$$

which is valid for $-\infty < z < +\infty$. Note that the acoustic pressure in Eq. (24) represents Rayleigh's second integral formula (cf. Williams [33], Eq. (2.67), p. 35), where the acoustic pressure on the plate is given in Eq. (40), and the derivative of the Green function for $z' = 0$ is presented earlier in Eq. (22). Now, assuming $e_f = 2$ and replacing $x, y$ with $x', y'$ in Eq. (13) yields

$$2p(x',y',0) = P(x'+a/2, y'+b/2) - \omega^2 \varrho h \left( k_D^{-4} \nabla'^4 - 1 \right) W(x'+a/2, y'+b/2), \tag{25}$$

where $\nabla'^4$ is the biharmonic operator with differentiation over the variables $x'$ and $y'$. Then, substituting Eq. (25) to Eq. (24) gives the acoustic pressure in the form of

$$p(\vec{r}) = \int_{S'} \left[ P(x'+a/2, y'+b/2) - \omega^2 \varrho h \left( k_D^{-4} \nabla'^4 - 1 \right) W(x'+a/2, y'+b/2) \right] \frac{\partial G(\vec{r},\vec{r}\,')}{\partial z'}\bigg|_{z'=0} \mathrm{d}S'. \tag{26}$$

Further, it can be obtained from the boundary condition in Eq. (15) that

$$\begin{aligned} \frac{\partial p}{\partial z}\bigg|_{z=0} &= \omega^2 \varrho_0 W(x+a/2, y+b/2) \\ &= \int_{S'} \left[ P(x'+a/2, y'+b/2) - \omega^2 \varrho h \left( k_D^{-4} \nabla'^4 - 1 \right) W(x'+a/2, y'+b/2) \right] \frac{\partial^2 G(\vec{r},\vec{r}\,')}{\partial z \partial z'}\bigg|_{z',z=0} \mathrm{d}S', \end{aligned} \tag{27}$$

for $0 < x < a$ and $0 < y < b$. Further

$$\frac{\partial^2 G(\vec{r},\vec{r}\,')}{\partial z \partial z'}\bigg|_{z',z=0} = \frac{\mathrm{i}}{8\pi^2} \int_{-\infty}^{+\infty} \int_{-\infty}^{+\infty} \mathrm{e}^{\mathrm{i}[k_x(x-x')+k_y(y-y')]} k_z \mathrm{d}k_y \mathrm{d}k_x. \tag{28}$$

Inserting Eqs. (17a), (17b), and (28), into Eq. (27) and applying Eq. (1) yields (cf. Eq. (7a))

$$\begin{aligned} &\omega^2 \varrho_0 \sum_n c_n W_n(x+a/2, y+b/2) \\ &= \sum_n \left[ \hat{P}_n - c_n \omega^2 \varrho h \left( \frac{k_n^4}{k_D^4} - 1 \right) \right] \frac{\mathrm{i}}{4\pi} \int_{-\infty}^{+\infty} \int_{-\infty}^{+\infty} \bar{W}_n(k_x,k_y) \mathrm{e}^{\mathrm{i}(k_x x + k_y y)} k_z \mathrm{d}k_y \mathrm{d}k_x. \end{aligned} \tag{29}$$

Now, multiplying Eq. (29) by $W_{n'}(x+a/2, y+b/2)$ integrating over the plate area, applying Eqs. (7a)–(8b), substituting $x + a/2 = u$ and $y + b/2 = v$, multiplying by $2\mathrm{i}/(\omega^2 \varrho h, k_0 ab)$, applying the orthogonality relation in Eq. (11), assuming that both sides of the plate are air-loaded ($e_f = 2$), and slightly rearranging results in

$$c_{n'} \mathrm{i}\varkappa - \sum_n c_n \left( \frac{k_n^4}{k_D^4} - 1 \right) \hat{\xi}_{nn'} = -\frac{1}{\omega^2 \varrho h} \sum_n \hat{P}_n \hat{\xi}_{nn'}, \tag{30}$$

where $n \equiv (q,p)$, $n' \equiv (q',p')$, the symbol * denotes the conjugate value, the dimensionless air loading coefficient is

$$\varkappa = \frac{e_f \varrho_0}{\varrho k_0 h}, \tag{31}$$

and the modal acoustic admittance coefficient is

$$\hat{\xi}_{nn'} = \frac{1}{ab} \int_{-\infty}^{+\infty} \int_{-\infty}^{+\infty} \bar{W}_n(k_x,k_y) \bar{W}_{n'}^*(k_x,k_y) \frac{k_z}{k_0} \mathrm{d}k_y \mathrm{d}k_x. \tag{32}$$

Now, the system of algebraic equations in Eq. (30) truncated for $n, n' = 1, 2, \ldots, N-1$ can be expressed in the matrix notation as follows (cf. Putra and Thompson [14] Eq. (C-3) in Appendix C)

$$\mathrm{i}\varkappa \mathbf{I} \cdot [c_{n'}] - [\hat{\xi}_{nn'}] \cdot [c_n (k_D^{-4} k_n^4 - 1)] = -(\omega^2 \varrho h)^{-1} [\hat{\xi}_{nn'}] \cdot [\hat{P}_n], \tag{33}$$

where the dot $\cdot$ denotes the scalar product, $\mathbf{I}$ is the identity matrix, and $[\hat{\xi}_{nn'}]$ is the square matrix, both of dimensions $N \times N$. $[c_{n'}]$, $[c_n(k_D^{-4} k_n^4 - 1)]$, and $[\hat{P}_n]$ are vectors of length $N$, while $\mathrm{i}\varkappa$ and $(\omega^2 \varrho h)^{-1}$ are scalar values. Then, multiplying Eq. (45) by the inverse matrix $[\hat{\xi}_{nn'}]^{-1}$ gives

$$\mathbf{I} \cdot [c_n (k_D^{-4} k_n^4 - 1)] - \mathrm{i}\varkappa [\hat{\lambda}_{nn'}] \cdot [c_{n'}] = (\omega^2 \varrho h)^{-1} \mathbf{I} \cdot [\hat{P}_n], \tag{34}$$

since $[\hat{\xi}_{nn'}]^{-1}\cdot\mathbf{I}=[\hat{\xi}_{nn'}]^{-1}$ and $[\hat{\xi}_{nn'}]^{-1}\cdot[\hat{\xi}_{nn'}]=\mathbf{I}$. The following square matrix has been introduced: $[\hat{\lambda}_{nn'}]=[\hat{\xi}_{nn'}]^{-1}$, where $[\hat{\xi}_{nn'}]^{-1}$ is the inverse matrix. Finally, the matrix equation in Eq. (34) can be expressed in its classical form as follows:

$$c_{n'}\left(\frac{k_{n'}^4}{k_D^4}-1\right)-\mathrm{i}\varkappa\sum_n c_n\hat{\lambda}_{nn'}=\frac{\hat{P}_{n'}}{\omega^2\varrho h}, \tag{35}$$

where the modal impedance coefficients $\hat{\lambda}_{nn'}$ are obtained from the inverse matrix $[\hat{\xi}_{nn'}]^{-1}$ of the modal acoustic admittance coefficients in Eq. (32).

The acoustic pressure in Eq. (26) can be rearranged by applying Eqs. (1) (to evaluate $\nabla'^4W_n(x'+a/2,y'+b/2)=k_n^4W_n(x'+a/2,y'+b/2)$), (17a), and (17b), and changing the order of summation and integration, giving

$$p(\vec{r})=\sum_n\left[\hat{P}_n-c_n\omega^2\varrho h\left(\frac{k_n^4}{k_D^4}-1\right)\right]\int_{S'}W_n(x'+a/2,y'+b/2)\frac{\partial G(\vec{r},\vec{r}\,')}{\partial z'}\bigg|_{z'=0}\mathrm{d}S'. \tag{36}$$

Differentiating the Green function in Eq. (22) once gives

$$\frac{\partial G(\vec{r},\vec{r}\,')}{\partial z'}\bigg|_{z'=0}=\mathrm{sign}(z)\frac{1}{8\pi^2}\int_{-\infty}^{+\infty}\int_{-\infty}^{+\infty}\mathrm{e}^{\mathrm{i}[k_x(x-x')+k_y(y-y')+k_z|z|]}\mathrm{d}k_y\mathrm{d}k_x, \tag{37}$$

since

$$\frac{\partial}{\partial z'}\mathrm{e}^{\mathrm{i}k_z|z-z'|}\bigg|_{z'=0}=-\mathrm{sign}(z)\mathrm{i}k_z\mathrm{e}^{\mathrm{i}k_z|z|}, \tag{38}$$

where $\mathrm{sign}(z)=1$ for $z>0$, $-1$ for $z<0$, and 0 for $z=0$ (the latter case is not applicable here as the Green function is not differentiable at $z=0$; the sign function is used only for convenience).

Applying Eq. (37) in Eq. (36), changing the order of integration, and using Eqs. (7a)–(8b) leads to

$$p(\vec{r})=\mathrm{sign}(z)\sum_n\left[\hat{P}_n-c_n\omega^2\varrho h\left(\frac{k_n^4}{k_D^4}-1\right)\right]\frac{1}{4\pi}\int_{-\infty}^{+\infty}\int_{-\infty}^{+\infty}\bar{W}_n(k_x,k_y)\mathrm{e}^{\mathrm{i}(k_xx+k_yy+k_z|z|)}\mathrm{d}k_y\mathrm{d}k_x. \tag{39}$$

Now, assuming $|z|\to 0$ and $e_f=2$, and applying the double inverse Fourier transform given in Eqs. (7b), (8c), and (8d), the acoustic pressure amplitude on the plate is obtained as

$$\lim_{\varepsilon\to 0}p(x,y,\pm\varepsilon)=\mathrm{sign}(z)\frac{1}{e_f}\sum_n\left[\hat{P}_n-c_n\omega^2\varrho h\left(\frac{k_n^4}{k_D^4}-1\right)\right]W_n(x+a/2,y+b/2). \tag{40}$$

The time-averaged acoustic power is (cf. Fahy and Gardonio [32], Eq. (3.100), p. 181)

$$\Pi=\int_{-a/2}^{+a/2}\int_{-b/2}^{+b/2}p(x,y,0)v^*(x+a/2,y+b/2)\mathrm{d}y\mathrm{d}x, \tag{41}$$

where the normal component of the sound intensity $p(x,y,0)v^*(x+a/2,y+b/2)$ is integrated over one side of the plate. The acoustic power radiated by the upper side is identical to that radiated by the lower side. Therefore, the integration in Eq. (41) is performed only over the upper side of the plate and then doubled, so the factor 1/2 from averaging cancels in Eq. (41). Applying Eqs. (16), (17a), and (40), and assuming $e_f=2$, gives

$$\Pi=\frac{1}{2}\mathrm{i}\omega ab\sum_n c_n^*\left[\hat{P}_n-c_n\omega^2\varrho h\left(\frac{k_n^4}{k_D^4}-1\right)\right]. \tag{42}$$

The reference acoustic power is (cf. Fahy and Gardonio [32], Eq. (3.102), p. 181)

$$\Pi_{\mathrm{Ref.}}=e_f\varrho_0 cab\left\langle|v|^2\right\rangle, \tag{43}$$

where the mean square vibration velocity on the plate is (cf. the orthogonality relation in Eq. (11))

$$\left\langle|v|^2\right\rangle=\frac{1}{2ab}\int_0^a\int_0^b|v(x,y)|^2\mathrm{d}y\mathrm{d}x=\frac{1}{2}\omega^2\sum_n|c_n|^2. \tag{44}$$

and $|c_n|^2=c_nc_n^*$. The radiation efficiency is (cf. Fahy and Gardonio [32] Eqs. (3.103) p. 181)

$$\sigma=\frac{\mathrm{Re}(\Pi)}{\Pi_{\mathrm{Ref.}}}. \tag{45}$$

Assuming that $\varrho_0\ll\varrho$ ($e_f\to 0$), the approximate resonant frequency of the air loaded plate can be expressed as follows (cf. Fahy and Gardonio [32] Eqs. (4.58) p. 268, Amabili et al. [34] Eqs. (8)–(10) and further details in Appendix C)

$$\omega'=\frac{\omega''}{\sqrt{1+\Gamma_n}}, \tag{46}$$

where $\omega''$ is the resonant frequency of the plate in vacuum, and the nondimensionalized added virtual mass incremental (NAVMI) is

$$\Gamma_n=-\varkappa\,\mathrm{Im}(\hat{\lambda}_{nn}). \tag{47}$$

It is worth noting that Eqs. (46) and (55) are consistent with the results presented by Fahy and Gardonio [32] (cf. their Eqs. (4.56)–(4.58)). As such, they are useful for both low and high frequencies. This method has also been applied to a vibrating elastically supported annular plate by Rdzanek et al. [35] and the fluid light loading effect has been discussed in their Sec. 2.8. On the other hand, the results presented by Amabili et al. [34] in their Eqs. (8)– (10) are valid only for low frequencies. The fluid effect on the resonant frequencies was analyzed numerically, and results obtained using the approach of Amabili et al. (called the Laplace equation approximation by Rdzanek et al.) were compared with those obtained using the approach of Rdzanek et al. (called the Helmholtz equation approximation by Rdzanek et al.). The approximation error is illustrated in their Figure 10d. The error increased almost linearly with frequency, reaching about 80 % for 5 kHz, while it did not exceed about 10 % for the same frequency.

### 2.5. The sound radiation of the excited vibrations of the plate in the RIB

The case of a plate vibrating in the RIB is the classical problem. Here, after some mathematical manipulations, Eq. (13) can be rearranged as

$$c_{n'}\left(\frac{k_{n'}^4}{k_D^4}-1\right)\mathrm{i}\varkappa\sum_n c_n\hat{\xi}_{nn'}=\frac{\hat{P}_{n'}}{\omega^2\varrho h}, \tag{48}$$

where the value of $\varkappa$ is obtained on the basis of Eq. (31) assuming $e_f=2$ (both sides of the plate are air loaded). Note that Eq. (48) has a form similar to Eq. (35).

The acoustic pressure amplitude can be expressed as

$$p(x,y,z)=\sum_{n=1}^{\infty}c_n p_n(x,y,z), \tag{49}$$

where the modal acoustic pressure is given by the following double inverse Fourier transform

$$p_n(x,y,z)=-\mathrm{i}\omega^2\varrho_0\frac{1}{2\pi}\int_{-\infty}^{+\infty}\int_{-\infty}^{+\infty}\bar{W}_n(k_x,k_y)\mathrm{e}^{\mathrm{i}(k_x x+k_y y+k_z z)}\frac{\mathrm{d}k_y\mathrm{d}k_x}{k_z}, \tag{50}$$

and $k_z^2=k_0^2-k_x^2-k_y^2$. The modal acoustic pressure amplitude in Eq. (50) can also be written as Rayleigh's first integral formula (cf. Williams [33] Eq. (2.75) p. 36)

$$p(x,y,z)=-\mathrm{i}\omega^2\varrho_0\int_{-a/2}^{+a/2}\int_{-b/2}^{+b/2}W(x'+a/2,y'+b/2)\frac{\mathrm{e}^{\mathrm{i}k_0R}}{\mathrm{i}2\pi R}\bigg|_{z'=0}\mathrm{d}y'\mathrm{d}x', \tag{51}$$

where $R^2=(x-x')^2+(y-y')^2+z^2$, by applying the Weyl integral for $z'=0$ (cf. Duffy [36] Eq. (4.5.27) p. 205; Williams [33] Eq. (2.64) p. 35).

The time-averaged acoustic power is

$$\Pi=\frac{e_f}{2}\int_0^a\int_0^b p(x,y,0)v^*(x+a/2,y+b/2)\mathrm{d}y\mathrm{d}x. \tag{52}$$

Inserting Eqs. (17a) and (49) to Eq. (52) gives

$$\Pi=\frac{e_f}{2}\varrho_0 c\omega^2 ab\sum_{n=1}^{\infty}\sum_{n'=1}^{\infty}c_n c_{n'}^*\hat{\xi}_{nn'}, \tag{53}$$

where the modal acoustic impedance coefficient is

$$\hat{\xi}_{nn'}=\frac{1}{ab}\int_{-\infty}^{+\infty}\int_{-\infty}^{+\infty}\bar{W}_n(k_x,k_y)\bar{W}_{n'}^*(k_x,k_y)\frac{k_0}{k_z}\,\mathrm{d}k_y\mathrm{d}k_x, \tag{54}$$

$\hat{\xi}_{nn'}=\hat{\xi}_{n'n}$, $\hat{\xi}_{nn'}=0$ if either $q+q'$ is odd or $p+p'$ is odd, and $\bar{W}_{n'}^*(k_x,k_y)$ is the conjugate value of $\bar{W}_n(k_x,k_y)$.

The acoustic pressure amplitude on the plate and the time-averaged acoustic power can be expressed in identical forms as in Eqs. (40) and (42). The only difference is that the coefficients $c_n$ assume different values. The NAVMI factor now takes the form (cf. Eq. (47))

$$\Gamma_n=-\varkappa\,\mathrm{Im}(\hat{\xi}_{nn}). \tag{55}$$

## 3. The spectral mapping for the admittance coefficients

In the case of the rectangular plate vibrating WNB, the modal admittance coefficients in Eq. (32) can be expressed, respectively, as follows (for more details see Appendix D)

$$\hat{\xi}_{nn'}=\frac{S_0}{S_{ab}}\sum_{\nu=0}^{\infty}\sum_{\nu'=0}^{\infty}\sum_{m=0}^{\infty}\epsilon_m\bar{N}_{\nu}^{|m|}\bar{N}_{\nu'}^{|m|}\bar{\xi}_{\nu\nu'}^{|m|}\,\mathrm{Re}\left[\hat{D}_n^{|m|}(\gamma_{\nu}^{|m|})\hat{D}_{n'}^{|m|*}(\gamma_{\nu'}^{|m|})\right], \tag{56}$$

where $\epsilon_0=1$, $\epsilon_m=2$ for $m=1,2,\ldots$, $\nu,\nu'=0,1,\ldots$, $S_0=\pi r_0^2$ ($r_0$ is the radius of the circle encircling the plate), $S_{ab}=ab$ is the plate's surface area, the eigenvalues $\gamma_{\nu}^{|m|}$ can be obtained on the basis of the characteristic equation $J_{|m|}(\gamma_{\nu}^{|m|}a)=0$, $\hat{\xi}_{n'n}=\hat{\xi}_{nn'}$, moreover $\hat{\xi}_{nn'}=$

0 if either $|q-q'|$ or $|p-p'|$ is odd ($n=(q,p)$ and $n'=(q',p')$), and the following relations have been used $k_z^2=k_0^2-\tau^2$, $k_x=\tau\cos\beta$, $k_y=\tau\sin\beta$, $x=r\cos\phi$, $y=r\sin\phi$, the complex expansion coefficient is (cf. Appendix A)

$$\hat{D}_n^{|m|}(\gamma_\nu^{|m|})=\frac{1}{2\pi}\int_{-a/2}^{+a/2}\int_{-b/2}^{+b/2}W_n(x+a/2,y+b/2)J_{|m|}(\gamma_\nu^{|m|}r)\mathrm{e}^{-\mathrm{i}|m|\phi}\mathrm{d}y\mathrm{d}x, \tag{57}$$

and the modal admittance coefficients are

$$\bar{\xi}_{\nu\nu'}^{|m|}=\frac{2}{r_0^2}\int_0^\infty \bar{D}_\nu^{|m|}(\tau)\bar{D}_{\nu'}^{|m|}(\tau)\frac{k_z}{k_0}\tau\mathrm{d}\tau. \tag{58}$$

Now, applying the following relation $k_z=(k_0^2-\tau^2)/k_z$ gives (cf. Lovat and Celozzi [37] Eq. (12))

$$\bar{\xi}_{\nu\nu'}^{|m|}=\left(1-\frac{(\gamma_\nu^{|m|})^2+(\gamma_{\nu'}^{|m|})^2}{2k_0^2}\right)\bar{\zeta}_{\nu\nu'}^{|m|}+\frac{\gamma_\nu^{|m|}}{2k_0}J_{|m|+1}(\gamma_\nu^{|m|}a)\bar{\zeta}_{1,\nu'}^{|m|}+\frac{\gamma_{\nu'}^{|m|}}{2k_0}J_{|m|+1}(\gamma_{\nu'}^{|m|}a)\bar{\zeta}_{1,\nu}^{|m|} \tag{59}$$

for any $|m|,\nu,\nu'=0,1,\ldots$, where the following integrals have been isolated (that can also be expressed in terms of rapidly convergent expansion series as below)

$$\bar{\zeta}_{1,\nu}^{|m|}=\frac{2}{k_0a}\int_0^\infty \bar{D}_\nu^{|m|}(\tau)J_{|m|}(\tau a)\frac{k_0}{k_z}\tau\mathrm{d}\tau=\sum_{\ell=0}^\infty \tilde{N}_\ell^{|m|}\tilde{D}_\ell^{|m|}(\gamma_\nu^{|m|})\tilde{\zeta}_{1,\ell}^{|m|}, \tag{60}$$

and the following integrals can be calculated exactly

$$\tilde{\zeta}_{1,0}^0=2\int_0^\infty J_1(\tau a)J_0(\tau a)\frac{\mathrm{d}\tau}{k_z}=\frac{1}{k_0a}\Big[1-J_0(2k_0a)-\mathrm{i}\boldsymbol{H}_0(2k_0a)\Big], \tag{61a}$$

$$\begin{aligned}\tilde{\zeta}_{1,\ell}^{|m|}&=\frac{2}{k_0a}\int_0^\infty \tilde{D}_\ell^{|m|}(\tau)J_{|m|}(\tau a)\frac{k_0}{k_z}\tau\mathrm{d}\tau=(-1)^\ell 2\int_0^\infty J_{|m|+2\ell+1}(\tau a)J_{|m|}(\tau a)\frac{\mathrm{d}\tau}{k_z}\\&=\frac{(-1)^\ell\Gamma^2(q+1)(k_0a)^{2q+1}}{\Gamma(q+p+2)\Gamma(m+1)\Gamma(2q+2)}\,{}_2F_3\big[q+1,q+1;q+p+2,m+1,2q+2;-(k_0a)^2\big]\\&\quad-\frac{4\mathrm{i}}{\pi(2p+1)(2q+1)}\,{}_3F_4\big[\tfrac12,\tfrac12,1;\tfrac12-p,p+\tfrac32,\tfrac12-q,q+\tfrac32;-(k_0a)^2\big],\end{aligned} \tag{61b}$$

with $p=\ell$ and $q=|m|+\ell$, and the modal impedance coefficients are given by

$$\bar{\zeta}_{\nu\nu'}^{|m|}=\frac{2}{r_0^2}\int_0^\infty \bar{D}_\nu^{|m|}(\tau)\bar{D}_{\nu'}^{|m|}(\tau)\frac{k_0}{k_z}\tau\mathrm{d}\tau=\sum_{\ell=0}^\infty\sum_{\ell'=0}^\infty \tilde{N}_\ell^{|m|}\tilde{D}_\ell^{|m|}(\gamma_\nu^{|m|})\tilde{\zeta}_{\ell\ell'}^{|m|}\tilde{N}_{\ell'}^{|m|}\tilde{D}_{\ell'}^{|m|}(\gamma_{\nu'}^{|m|}) \tag{62a}$$

$$\bar{\zeta}_{\nu\nu}^{|m|}=\sum_{\ell=0}^\infty(\tilde{N}_\ell^{|m|})^2[\tilde{D}_\ell^{|m|}(\gamma_\nu^{|m|})]^2\tilde{\zeta}_{\ell\ell}^{|m|}+2\sum_{\ell=1}^\infty\sum_{\ell'=\ell+1}^\infty \tilde{N}_\ell^{|m|}\tilde{D}_\ell^{|m|}(\gamma_\nu^{|m|})\tilde{\zeta}_{\ell\ell'}^{|m|}\tilde{N}_{\ell'}^{|m|}\tilde{D}_{\ell'}^{|m|}(\gamma_\nu^{|m|}) \tag{62b}$$

$$\tilde{\zeta}_{\ell\ell'}^{|m|}=\frac{2}{r_0^2}\int_0^\infty \tilde{D}_\ell^{|m|}(\tau)\tilde{D}_{\ell'}^{|m|}(\tau)\frac{k_0}{k_z}\tau\mathrm{d}\tau=-\lim_{J\to\infty}\sum_{j=1}^J\frac{(-\frac12 j)_p(-\frac12 j+1)_q(\mathrm{i}k_0r_0)^j}{\Gamma(\frac12 j+p+1)\Gamma(\frac12 j+q+2)}, \tag{62c}$$

$$\bar{D}_\nu^{|m|}(\tau)=\frac{J_{|m|}(\tau r_0)}{(\gamma_\nu^{|m|})^2-\tau^2}\gamma_\nu^{|m|}r_0J_{|m|+1}(\gamma_\nu^{|m|}r_0),\qquad \tilde{D}_\ell^{|m|}(\tau)=(-1)^\ell\frac{r_0}{\tau}J_{|m|+2\ell+1}(\tau r_0), \tag{62d}$$

$$(\tilde{N}_\nu^{|m|})^{-1}=\frac{r_0^2}{2}J_{|m|+1}^2(\gamma_\nu^{|m|}a),\qquad \tilde{N}_\ell^{|m|}=\frac{2}{r_0^2}(|m|+2\ell+1), \tag{62e}$$

with $p=\ell'-\ell$ and $q=|m|+\ell'+\ell$, $k_z^2=k_0^2-\tau^2$, the Pochhammer symbol is $(a)_n=\Gamma(a+n)/\Gamma(a)$ (cf. Abramowitz and Stegun [38] Eq. 6.1.22). It is worth mentioning that the quantity presented in Eq. (62a) is similar to the modal radiation impedance coefficients of a stretched circular membrane (cf. Morse and Ingard [39] Eq. (10.2.14)) and Fig. (10.8); and Rdzanek et al. [40] Eq. (15) and (25b)). The expansion series in Eq. (62c) is accurate and highly convergent for $ka\leqslant 12$ and $J\geqslant 10+2\mathrm{e}ka$ ($\mathrm{e}\sim 2.718$), where the relative percentage error is smaller than $10^{-4}$ % (cf. Aarts and Janssen [41] in their Eq. (A24)). In addition, for the rectangular plate vibrating in the RIB, the modal impedance coefficients $\hat{\zeta}_{n,n'}$ in Eqs. (54) can be obtained from Eq. (56) simply by replacing $\bar{\xi}_{\nu\nu'}^{|m|}$ with $\bar{\zeta}_{\nu\nu'}^{|m|}$.

The expansion in Eq. (62a) is useful for numerical calculations, whether $\nu=\nu'$ or $\nu\neq\nu'$. In the case when $\nu\neq\nu'$, the integral in Eq. (62a) can be rearranged using the following basic relation

$$\frac{1}{(\gamma_\nu^{|m|})^2-\tau^2}\,\frac{1}{(\gamma_{\nu'}^{|m|})^2-\tau^2}=\frac{1}{(\gamma_\nu^{|m|})^2-(\gamma_{\nu'}^{|m|})^2}\left[\frac{1}{(\gamma_{\nu'}^{|m|})^2-\tau^2}-\frac{1}{(\gamma_\nu^{|m|})^2-\tau^2}\right], \tag{63}$$

which leads to

$$\bar{\zeta}_{\nu\nu'}^{|m|}=\frac{k_0}{(\gamma_\nu^{|m|})^2-(\gamma_{\nu'}^{|m|})^2}\left[\gamma_\nu^{|m|}J_{|m|+1}(\gamma_\nu^{|m|}a)\bar{\xi}_{1,\nu'}^{|m|}-\gamma_{\nu'}^{|m|}J_{|m|+1}(\gamma_{\nu'}^{|m|}a)\bar{\xi}_{1,\nu}^{|m|}\right], \tag{64}$$

where $\nu, \nu' = 0, 1, \ldots$, $k_z^2 = k_0^2 - \tau^2$, the eigenvalues $\gamma_\nu^{|m|}$ are obtained from the characteristic equation $J_{|m|}(\gamma_\nu^{|m|} a) = 0$.

The complex expansion coefficient in Eq. (57) can be expressed as

$$\begin{aligned}\hat{D}_n^{|m|}(\gamma_\nu^{|m|}) = \frac{ab}{16\pi}\Bigg\{ & \hat{\hat{D}}_{|m|,q}(\gamma_\nu^{|m|}a/2)\tilde{\tilde{D}}_{0,p}(\gamma_\nu^{|m|}b/2) + \sum_{\mu=1}^{\infty}(-\mathrm{i})^\mu\left[\hat{\hat{D}}_{|m|+\mu,q}(\gamma_\nu^{|m|}a/2) + \hat{\hat{D}}_{|m|-\mu,q}(\gamma_\nu^{|m|}a/2)\right]\tilde{\tilde{D}}_{\mu,p}(\gamma_\nu^{|m|}b/2)\Bigg\} \\ & + \frac{ab}{16\pi}(-\mathrm{i})^{|m|}\Bigg\{\hat{\hat{D}}_{0,q}(\gamma_\nu^{|m|}a/2)\tilde{\tilde{D}}_{|m|,p}(\gamma_\nu^{|m|}b/2) \\ & + \sum_{\mu=1}^{\infty}\mathrm{i}^\mu\hat{\hat{D}}_{\mu,q}(\gamma_\nu^{|m|}a/2)\left[\tilde{\tilde{D}}_{|m|+\mu,p}(\gamma_\nu^{|m|}b/2) + \tilde{\tilde{D}}_{|m|-\mu,p}(\gamma_\nu^{|m|}b/2)\right]\Bigg\},\end{aligned} \tag{65}$$

where $\hat{D}_n^{m*}(\gamma_\nu^{|m|})$ can be obtained as the conjugate value of $\hat{D}_n^{m}(\gamma_\nu^{|m|})$,

$$\hat{\hat{D}}_{\mu,q}(\gamma_\nu^{|m|}a/2) = \sum_{\mu'=0}^{\infty}\hat{T}_{2\mu'+\bar{\beta}(\mu),q}\hat{\hat{D}}_{\mu,\mu'}(\gamma_\nu^{|m|}a/2), \tag{66a}$$

$$\tilde{\tilde{D}}_{\mu,p}(\gamma_\nu^{|m|}b/2) = \sum_{\mu'=0}^{\infty}\tilde{T}_{2\mu'+\bar{\beta}(\mu),p}\hat{\hat{D}}_{\mu,\mu'}(\gamma_\nu^{|m|}b/2), \tag{66b}$$

for odd $\mu + q$ and $\mu + p$ and zero otherwise, and

$$\hat{\hat{D}}_{\mu,\mu'}(\xi) = \mathrm{i}^{|\mu|-\mu}\epsilon_{\bar{\beta}(|\mu|)+\mu'}J_{\lceil|\mu|/2\rceil+\mu'}(\xi/2)J_{\bar{\alpha}(|\mu|)-\mu'}(\xi/2), \tag{67}$$

with $\xi$ being either $\gamma_\nu^{|m|}a/2$ or $\gamma_\nu^{|m|}b/2$, $\bar{\alpha}(\mu) = \mathrm{Integer}(\mu/2)$ being the integer part of dividing an integer value $\mu$ by 2 and $\bar{\beta}(\mu) = \mathrm{Rest}(\mu/2)$ being the rest of dividing an integer value $\mu$ by 2, $\mathrm{i}^{|\mu|-\mu} = 1$ for $\mu = 0, 1, .$, $\mathrm{i}^{|\mu|-\mu} = (-1)^\mu$ for $\mu = -1, -2, .$, and $\lceil|\mu|/2\rceil = \bar{\alpha}(|\mu|) + \bar{\beta}(|\mu|)$ ($\lceil x\rceil$ is the smallest integer greater equal $x$).

The coefficients $\hat{T}_{\mu,q}$ and $\tilde{T}_{\mu,p}$ occurring in Eqs. (66a) and (66b) can be obtained on the basis of the following rapidly converging expansion series

$$\begin{aligned}\hat{T}_{\mu,q} = {} & \hat{A}_{1,q}^{(c)}\sum_{r=0}^{\lfloor\mu/2\rfloor}\tilde{\alpha}_{\mu,2r}\left[(-1)^r j_{2r}(\alpha_{1,q}a/2) - \frac{i_{2r}^{(1)}(\alpha_{2,q}a/2)}{\cosh(\alpha_{2,q}a/2)}\cos(\alpha_{1,q}a/2)\right] \\ & - \hat{A}_{1,q}^{(s)}\sum_{r=0}^{\lfloor\mu/2\rfloor}\tilde{\alpha}_{\mu,2r+1}\left[(-1)^r j_{2r+1}(\alpha_{1,q}a/2) - \frac{\alpha_{1,q}}{\alpha_{2,q}}\frac{i_{2r+1}^{(1)}(\alpha_{2,q}a/2)}{\cosh(\alpha_{2,q}a/2)}\cos(\alpha_{1,q}a/2)\right],\end{aligned} \tag{68a}$$

$$\begin{aligned}\tilde{T}_{\mu,p} = {} & \tilde{A}_{2,p}^{(c)}\sum_{r=0}^{\lfloor\mu/2\rfloor}\tilde{\alpha}_{\mu,2r}\left[(-1)^r j_{2r}(\beta_{1,p}b/2) - \frac{i_{2r}^{(1)}(\beta_{2,p}b/2)}{\cosh(\beta_{2,p}b/2)}\cos(\beta_{1,p}b/2)\right] \\ & - \tilde{A}_{2,p}^{(s)}\sum_{r=0}^{\lfloor\mu/2\rfloor}\tilde{\alpha}_{\mu,2r+1}\left[(-1)^r j_{2r+1}(\beta_{1,p}b/2) - \frac{\beta_{1,p}}{\beta_{2,p}}\frac{i_{2r+1}^{(1)}(\beta_{2,p}b/2)}{\cosh(\beta_{2,p}b/2)}\cos(\beta_{1,p}b/2)\right],\end{aligned} \tag{68b}$$

where $\lim_{u\to\infty}[i_r^{(1)}(u)/\cosh(u)] = 0$ for $r = 0, 1, \ldots$, and

$$\hat{A}_{1,q}^{(c)} = 2A_{1,q}f_{1,q}(a/2), \qquad \hat{A}_{1,q}^{(s)} = 2A_{1,q}g_{1,q}(a/2), \tag{69a}$$

$$\tilde{A}_{2,p}^{(c)} = 2A_{2,p}f_{2,p}(b/2), \qquad \tilde{A}_{2,p}^{(s)} = 2A_{2,p}g_{2,p}(b/2), \tag{69b}$$

In the specific case when $\mu = 0$, $T_0(u) = 1$ and

$$\hat{T}_{0,q} = \frac{4A_{1,q}}{\alpha_{1,q}a}\left\{\left(1 + \frac{\alpha_{1,q}^2}{\alpha_{2,q}^2}\frac{\cos(\alpha_{1,q}a/2)}{\cosh(\alpha_{2,q}a/2)}\right)g_{1,q}(a/2) - \frac{2k_n^2\bar{k}_{1,q}}{\alpha_{1,q}\alpha_{2,q}}\right\}; \quad q = 1, 3, \ldots, \tag{70a}$$

$$\tilde{T}_{0,p} = \frac{4A_{2,p}}{\beta_{1,p}b}\left\{\left(1 + \frac{\beta_{1,p}^2}{\beta_{2,p}^2}\frac{\cos(\beta_{1,p}b/2)}{\cosh(\beta_{2,p}b/2)}\right)g_{2,p}(b/2) - \frac{2k_n^2\bar{k}_{2,p}}{\beta_{1,p}\beta_{2,p}}\right\}; \quad p = 1, 3, \ldots. \tag{70b}$$

The detailed derivation of Eqs. (68a)–(70b) has been presented in the Supplementary Material. It is worth noting that the expansion coefficients in Eq. (65) are essentially values independent on frequency. Therefore, they can be calculated a priori and later used for calculations in Eq. (56) for arbitrary frequency, which helps to improve the time efficiency of numerical calculations.

**Table 1**
The selected resonant frequencies $f_r$ and the eigenfrequencies $f_n$ of the plate of the sizes $0.60\,\mathrm{m} \times 0.50\,\mathrm{m} \times 3.0\,\mathrm{mm}$ and the critical frequency $f_c = 3980.1\,\mathrm{Hz}$ (cf. Eq. (71)), where $\Gamma_n$ is the NAVMI factor (cf. Eq. (55)). Key for results obtained: ta—using TAFM, fe—using FEM, wb—from the Warburton approximation (cf. Warburton [15] Eqs. (15) and (16), Squicciarini et al. [43] Eq. (4), and Leissa [44] Eq. (4.16)), and na—using the NAVMI factors (cf. Eq. (46)).

| Index | | | Vacuum | | | Air, Infinite Baffle | | | | Air, No Baffle | | | |
|---|---|---|---|---|---|---|---|---|---|---|---|---|---|
| $n$ | $q$ | $p$ | $f_{n,\mathrm{ta}}$(Hz) | $f_{n,\mathrm{fe}}$(Hz) | $f_{n,\mathrm{wb}}$(Hz) | $f_{r,\mathrm{ta}}$(Hz) | $f_{r,\mathrm{fe}}$(Hz) | $f_{r,\mathrm{na}}$(Hz) | $\Gamma_n$ | $f_{r,\mathrm{ta}}$(Hz) | $f_{r,\mathrm{fe}}$(Hz) | $f_{r,\mathrm{na}}$(Hz) | $\Gamma_n$ |
| 1 | 1 | 1 | 90.0719 | 92.292 | 92.4782 | 87.5 | 90.0 | 88.817 | 0.028452 | 88.5 | 90.8 | 88.988 | 0.024518 |
| 2 | 2 | 1 | 164.942 | 166.83 | 170.923 | 162.5 | 165.6 | 162.775 | 0.026811 | 163.0 | 165.8 | 163.117 | 0.022507 |
| 3 | 1 | 2 | 206.378 | 207.67 | 211.090 | 203.5 | 206.7 | 204.325 | 0.020198 | 204.0 | 207.0 | 204.514 | 0.018307 |
| 4 | 2 | 2 | 274.096 | 276.32 | 294.435 | 271.5 | 276.5 | 271.403 | 0.019940 | 271.5 | 276.4 | 271.529 | 0.018997 |
| 5 | 3 | 1 | 285.567 | 286.92 | 290.847 | 283.0 | 287.0 | 283.089 | 0.017581 | 283.0 | 287.0 | 283.244 | 0.016467 |
| 47 | 7 | 5 | 1943.98 | 1943.4 | 1998.91 | 1935.0 | – | 1935.90 | 0.008360 | 1935.0 | – | 1935.52 | 0.008760 |
| 48 | 9 | 2 | 1976.77 | 1974.9 | 2010.86 | 1969.0 | – | 1968.13 | 0.008798 | 1968.0 | – | 1968.10 | 0.008830 |
| 49 | 8 | 4 | 1984.16 | 1983.0 | 2036.17 | – | – | 1975.83 | 0.008450 | – | – | 1975.37 | 0.008924 |
| 50 | 4 | 7 | 1998.30 | 1997.2 | 2041.42 | 1990.0 | – | 1988.98 | 0.009386 | 1989.5 | – | 1989.29 | 0.009075 |
| 51 | 6 | 6 | 2012.41 | 2011.7 | 2066.68 | 2003.5 | – | 2004.35 | 0.008054 | 2003.5 | – | 2004.13 | 0.008277 |

## 4. Numerical analysis

The numerical analysis has been carried out methodically in a step-by-step manner to apply sample calculations using the TAFM. This method incorporates the exact results presented in this study and in Section 3. The numerical results obtained are further validated using the FEM. It should also be noted that the relation between the double inverse Fourier transforms and the series of single inverse Hankel transforms, as discussed by Cornacchio and Soni [24] and Baddour [25], has been applied to the majority of the numerical calculations presented herein. The rigorous application of this relation is demonstrated in Section 3. In general, the Dini coefficients should be integrated over the surface area of the circle. In the present case, the radius of this circle should be equal to half of the diagonal of the rectangular plate. Nevertheless, the integration in Eqs. (65) and (66a) can be restricted to the surface area of the rectangular plate, since either the normal vibration velocity of the plate is equal to zero (for the Neumann boundary condition) or the acoustic pressure is zero (for the Dirichlet boundary condition) on the circle outside the rectangular plate. Therefore, the application of the above-mentioned relation is justified herein. This application makes it possible to perform all numerical calculations without further simplifications. All modal admittance coefficients are included in the calculations, and thus the results are highly accurate, while the computational cost remains reasonable. In other words, without applying the relation proposed by Cornacchio and Soni [24], most of the results presented here would not be achievable through direct numerical integration in Eqs. (54) and (32).

In this study, it is assumed that the plate is air-loaded on both sides. Consequently, $e_f = 2$ throughout the numerical analysis. The plate is submerged in air with an ambient density $\varrho_0 = 1.2\,\mathrm{kg/m^3}$. The speed of sound is $c = 343\,\mathrm{m/s}$. The plate is made of aluminum, with the following parameter values: $\varrho_p = 2700\,\mathrm{kg/m^3}$, $E = 71\,\mathrm{GPa}$, $\nu = 0.33$, and $\eta = 10^{-4}$. The dimensions of the plate are $a = 0.60\,\mathrm{m}$, $b = 0.50\,\mathrm{m}$, and the thickness is $3.0\,\mathrm{mm}$. The critical frequency is given by

$$f_c = \frac{c^2}{2\pi}\sqrt{\frac{\varrho_p h}{D_E}}, \tag{71}$$

which yields a value of $f_c = 3980.1\,\mathrm{Hz}$ for the considered plate.

The first step is to numerically determine the eigenfrequencies of the plate using the equations from Section 2.2. They were obtained using the Python function 'findroot' with the 'anderson' solver from the 'mpmath' library [42]. The calculations were performed for modal numbers $q$ and $p$ in Eq. (3a) ranging from 1 to 50, resulting in a total of 2500 eigenfrequencies. These eigenfrequencies were then sorted in ascending order and numbered as $n = 1, \ldots, 2500$. This number is far more than necessary, as only the first 283 eigenfrequencies are below 10 kHz. Even when an additional 60 modes are included, this results in 343 modes (up to eigenfrequency $f_{343} = 11.9368\,\mathrm{kHz}$ for $q = 21$ and $p = 9$), which are sufficient for calculating the reference values (used to assess approximation errors). Nevertheless, a larger set of eigenfrequencies was calculated to ensure that none of the first 343 were omitted. The flowchart of the numerical calculation scheme is presented in Appendix E.

Some representative eigenfrequencies are provided in Table 1, together with values obtained using FEM and the Warburton approximation (cf. Warburton [15]) and (16), Squicciarini et al. [43] Eq. (4)). It can be observed that the FEM results agree well with those presented herein, and the difference between both methods does not exceed 1 Hz for the 51st eigenfrequency. On the other hand, the Warburton approximation is consistent for the lowest eigenfrequencies, while significant divergence appears at higher eigenfrequencies. For example, the Warburton result is overestimated by about 55 Hz compared to the results from FEM and the formulas used herein for the 51st eigenfrequency, indicating that it is accurate only for the lowest eigenfrequencies. Table 1 also provides the values of the resonant frequencies estimated using the NAVMI factor based on Eqs. (46), (47), and (55). These estimates agree very well with the values obtained by solving the system of algebraic equations in Eqs. (35) and (48).

The lowest eigenfunctions are illustrated in Fig. 2(a) and (b) for the modal numbers $q, p = 1, \ldots, 7$, and the excitation coordinates $x = 0.24a$ and $y = 0.24b$ were selected to avoid exciting the nodal lines of these modes. The coordinates are indicated with vertical red dotted lines in Figs. 2(a) and (b). Such a selection of the excitation point ensures that all resonant maxima occur at each successive

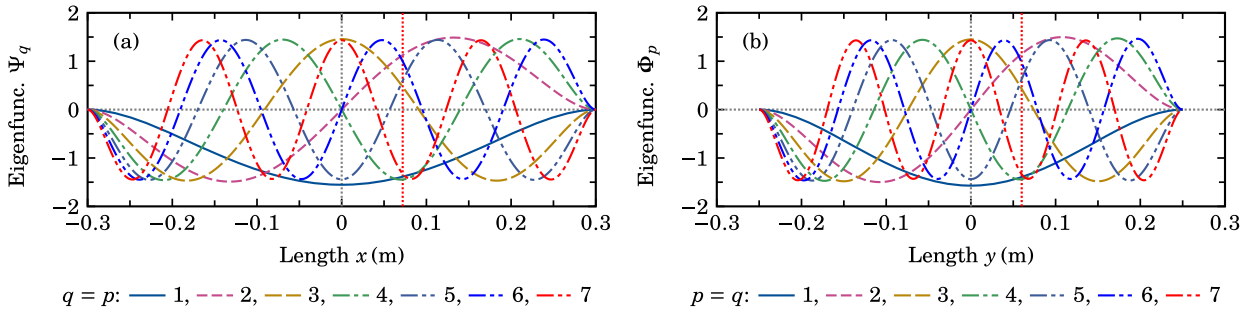


**Fig. 2.** The selected initial eigenfunctions $\Psi_q(x)$ and $\Phi_p(y)$ on the plate for $q = p = 1, \ldots, 7$. The coordinates $x = 0.24a$ and $y = 0.24b$ of the excitation point (vertical red dotted lines) were selected to avoid any nodal lines for these eigenfunctions. (For interpretation of the references to colour in this figure legend, the reader is referred to the web version of this article.)

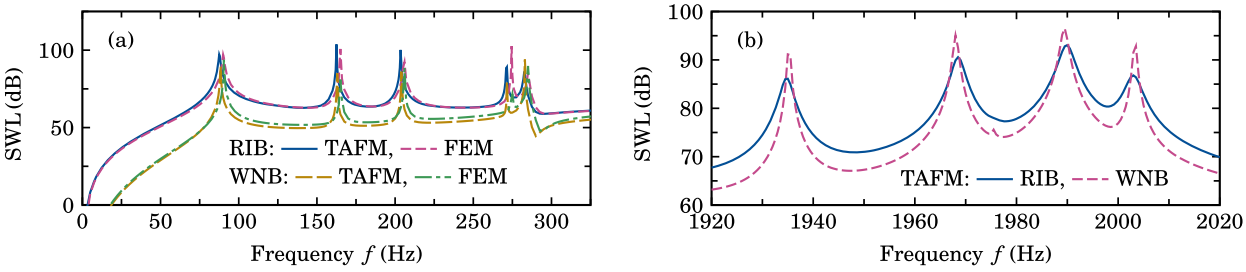


**Fig. 3.** Comparison of the SWL (dB) of the plate excited at low frequencies by a concentrated load at $(0.24a, 0.24b)$ obtained using TAFM and FEM for the plate: (a) in the RIB, (b) WNB.

resonant frequency as long as the specified mode number intervals are not exceeded. Therefore, it can be expected that choosing excitation frequencies at the five lowest resonant frequencies (i.e., below 286 Hz) will result in resonant responses. This reasoning is confirmed by the results presented in Fig. 3(a), where five maxima of the sound power level SWL$= 10\log_{10}(\Pi/\Pi_0)$ of the vibrating plate can be observed, whether the plate is embedded into the RIB or is WNB, where $\Pi$ is the acoustic power and $\Pi_0 = 1$ pW is the reference value. It can be noted that the results obtained using TAFM and those from FEM are generally in good agreement. The SWL for the plate in the RIB is greater by about 10 to 20 dB than the SWL for the plate in WNB for all frequencies below 330 Hz except at the resonant frequencies. At the resonant frequencies, the SWL assumes comparable values whether the plate is in the RIB or WNB. The five resonant maxima can be observed at the frequencies specified in Table 1 below 330 Hz. The resonant frequencies are slightly lower when the plate is in the RIB compared with the case of WNB. The TAFM results are obtained by incorporating all necessary modes for $n = 1, \ldots, N$ in the numerical analysis for a given excitation frequency smaller than or equal to 4 kHz, where $f_N$ is the highest eigenfrequency smaller than or equal to the excitation frequency $f$. After the number of necessary modes is determined, it is increased by the mode number increment (MNI) $\Delta N$ to improve the accuracy of the results. In this figure, the MNI was selected arbitrarily as $\Delta N = 10$, as this value was anticipated to be sufficient. The relation between the MNI, approximation errors, and computational efficiency will be discussed later. On the other hand, FEM requires a sufficiently large region around the plate and a perfectly matched layer (PML) to ensure reasonable results. It was assumed that the largest finite element does not exceed one sixth of the excitation wavelength. This requirement is satisfied for frequencies up to 150 Hz in Fig. 3(a), which means that the FEM results obtained for higher frequencies should be interpreted with caution. Meeting this requirement up to 300 Hz would result in about $(300/150)^3 = 8$ times more finite elements, which was not feasible with the computer used. The FEM results are not presented in Fig. 3(b) for the same reason. In this figure the requirement of at least six finite elements per wavelength for frequencies up to 2 kHz would result in an approximate number of elements about $(2000/150)^3 = 2370$ times higher than in Fig. 3(a). In addition, the COMSOL software generates the mesh automatically and provides elements that are much smaller near the plate, especially along its edges when the plate is WNB. The elements on the plate are also smaller, as the bending wavenumbers on the plate are shorter than the acoustic wavelengths below the critical frequency $f_c = 3980.1$ Hz. The free region is chosen as a full sphere with a radius six times the diagonal of the plate. The thickness of the PML is also six times this diagonal. All these factors lead to a huge number of finite elements in the acoustic field simulations, making the calculations very time-consuming. A total of 132 frequency samples were calculated using both TAFM and FEM. Additional samples were added near the resonant frequencies to make the curves in Fig. 3(a) acceptably smooth.

The SWL maxima for higher frequencies are presented in Fig. 3(b), covering the frequency interval from 1920 to 2020 Hz, which contains the five eigenfrequencies listed in the lower part of Table 1. Only four resonant maxima can be observed because the excitation point lies on one of the nodal lines of the 49th mode. Consequently, the 49th mode of the plate is not excited and its resonant maximum is absent for this mode. The difference in SWL does not exceed about 5 dB within this frequency interval for the

**Table 2**
The mean ratio of the time required for calculations of the averaged acoustic power $\Pi_{\text{Avg.}}$ (W) per frequency sample for frequencies smaller than 330 Hz using two different methods, TIFM and FEM, with the reference time obtained using the TAFM.

| | $\frac{t_{\text{TIFM}}}{t_{\text{TAFM}}}$ | $\frac{t_{\text{FEM}}}{t_{\text{TAFM}}}$ |
|---|---|---|
| Infinite Baffle | 2.435 | 1.967 |
| No Baffle | 2.555 | 1.962 |

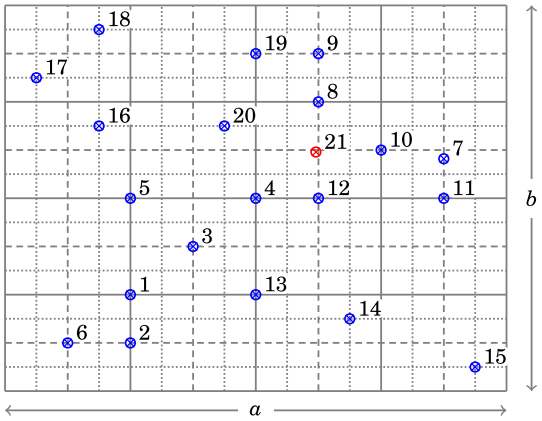


**Fig. 4.** The selected 21 excitation points on the plate (cf. Putra and Thompson [14] Fig. 1).

plates in the RIB and WNB. The SWL is still higher for the plate in the RIB, except at the resonant frequency, where the SWL for the plate in WNB is greater. It was not possible to obtain FEM results with acceptable accuracy in this frequency interval using a regular computer; therefore, such results are not presented in Fig. 3(b) or in Table 1.

Table 2 presents the ratio of the mean time required for numerical calculations of the averaged acoustic power $\Pi_{\text{Avg.}}$ (W) per frequency sample for frequencies below 330 Hz, using the theoretical integration formulas method (TIFM) and TAFM, where the latter provides the reference time. This ratio measures the time efficiency of the TAFM compared with TIFM and FEM. On average, the TAFM is about 2.5 times more time-efficient than TIFM and about 2 times more efficient than FEM. With respect to TIFM, there are at least two major issues. First, the numerical integration procedure 'NIntegrate' in Mathematica fails to compute the double integrals in Eqs. (54) and (32), becoming ineffective for some frequencies above 330 Hz. Second, it is difficult to control the accuracy of double numerical integration, and this becomes impossible when the procedure fails. The second column of values in Table 2 shows the ratio of the time required for calculations using FEM compared with TAFM. The ratio is close to 2. The main problem with FEM is that the number of finite elements required for calculations grows rapidly with frequency. As a result, physically correct results can be obtained only for frequencies below 150 Hz, which is far below the plate's critical frequency. This is a very narrow interval of low frequencies, and the results obtained using FEM are useful mainly for validation of the TAFM. In contrast, the TAFM is free from these shortcomings. It enables numerical calculations up to 10 kHz, which is well above the critical frequency of the plate. At the same time, the accuracy can be controlled by selecting greater or smaller MNI. It should be emphasized that the TAFM allows further optimization of time efficiency. For example, once the modal admittance coefficients are calculated, they can be reused for rapid calculations at different excitation points. In contrast, any change in the excitation point requires repeating time-consuming calculations using FEM. Consequently, the acoustic power averaged over 20 excitation points can be obtained about 40 times faster using TAFM than FEM since the modal admittance coefficients need to be calculated only once .

The sound power level is $\text{SWL}_{\text{Avg.}} = 10\log_{10}(\Pi_{\text{Avg.}}/\Pi_0)$ for the plate vibrating either in the RIB or WNB, where $\Pi_{\text{Avg.}}$ is the acoustic power $\Pi$ averaged over the 21 different excitation points shown in Fig. 4 and $\Pi_0 = 1$ pW. The excitation points were selected after Putra and Thompson [14] (cf. their Figure 1) to ensure that as many resonant maxima as possible are obtained across a wide frequency range, from the lowest values to well above the critical frequency. The 21st excitation point was added to ensure that all resonant maxima are captured for frequencies below 330 Hz.

The SWL presented in Fig. 5(a) is generally greater for the plate in the RIB than for the plate in WNB. The difference is about 20 dB around the fundamental frequency and decreases to zero as the frequency approaches the critical value. Fig. 5(b) shows the radiation efficiency for both plates and demonstrates that the plate in WNB is a much weaker radiator than the plate in the RIB below the critical frequency. This conclusion is consistent with the findings of Laulagnet [5] (cf. Figs. 5, 7, and 9), Putra and Thompson [14] (cf. Figs. 8 and 9), Bao et al. [45] (cf. Fig. 5), and Neekar et al. [46] (cf. Figs. 1, 3, and A2). Fig. 5(c) presents the mean square

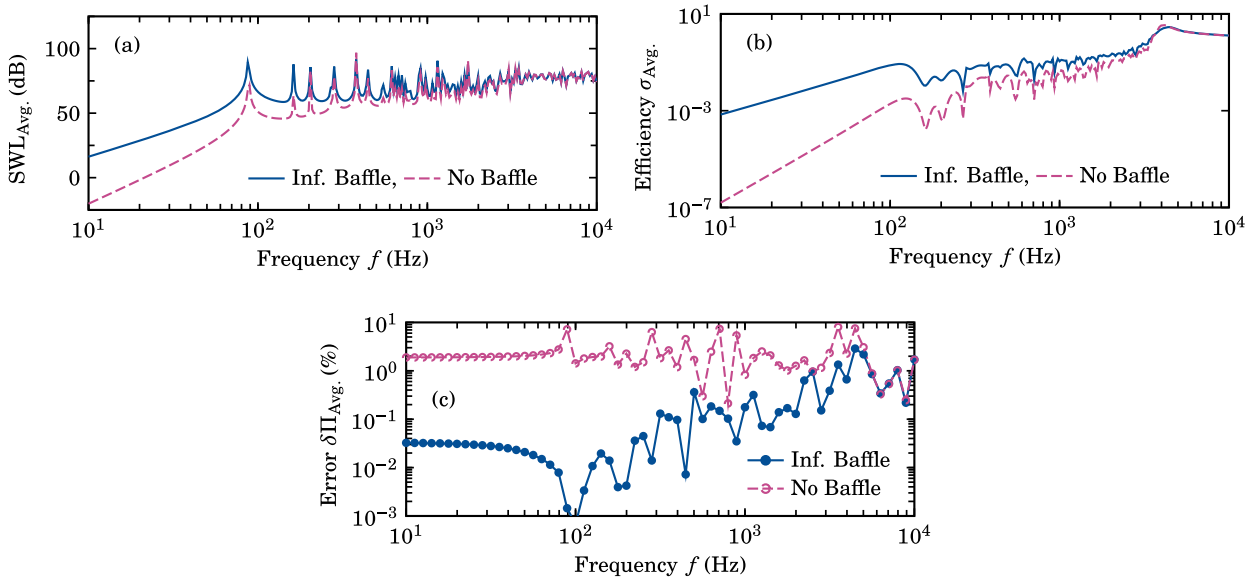


**Fig. 5.** (a) The SWL$_{Avg.}$ for the acoustic power $\Pi_{Avg.}$ averaged over all 21 excitation points shown in Fig. 4 (cf. Putra and Thompson [14] Fig. 2, thin curves) for $\Delta N = 10$. (b) The radiation efficiency $\sigma_{Avg.}$ averaged over all the same 21 excitation points for $\Delta N = 10$. (c) The approximation error for the averaged acoustic power $\delta\Pi_{Avg.}$ (%) for $\Delta N = 10$ with the reference values obtained for $\Delta N = 40$.

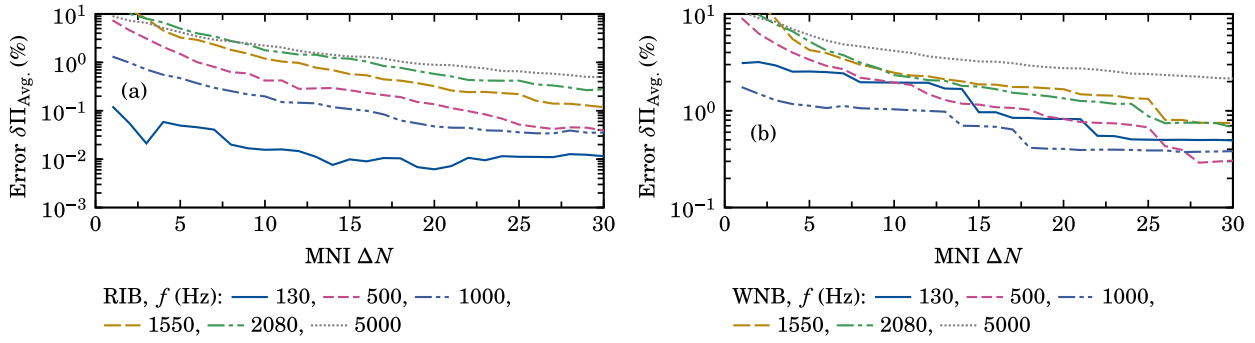


**Fig. 6.** The approximation error $\delta\Pi_{Avg.}$ (%). for the averaged acoustic power $\Pi_{Avg.}$ over all 21 excitation points shown in Fig. 3 (cf. Putra and Thompson [14], Fig. 2, thin curves) as a function of $\Delta N$ with the reference values calculated for $\Delta N = 60$ for arbitrarily selected frequencies for the plate in the RIB and WNB.

approximation error

$$\delta\Pi_{Avg.} = \left\{ \frac{1}{\Delta f} \int_{f_1}^{f_2} \frac{|\Pi_1 - \Pi_2|^2}{|\Pi_2|^2} \, \mathrm{d}f \right\}^{1/2} 100\,\%, \tag{72}$$

averaged over the frequency interval from $f_1 = 10\,\mathrm{Hz}$ to $f_2 = 10\,\mathrm{kHz}$, where $\Delta f = f_2 - f_1$, $\Pi_1 = \Pi_{Avg.}$ is the acoustic power $\Pi$ averaged over the 21 excitation points shown in Fig. 4 and calculated for $\Delta N = 10$, and the reference value $\Pi_2 = \Pi_{Avg.}$ is calculated for $\Delta N = 40$. The error does not exceed 4 % for the plate in the RIB and reaches its maximum around the critical frequency. For the plate in WNB the error is generally larger but does not exceed 10 %. It reaches local maxima at the resonant frequencies. The question arises as to what causes these local maxima for the plate in WNB, which do not occur for the plate in RIB. This issue will be addressed later.

Although all the theoretical formulas used in this study are exact, some numerical errors are inevitable. The primary source of these errors is truncation in the eigenfunction expansion for the transverse displacement of the plate and the excitation in Eqs. (17a) and (17b). As mentioned before, all the necessary eigenfunctions are included (up to the excitation frequency) in these expansions, and then the number of eigenfunctions is increased by the factor MNI to improve accuracy and minimize numerical errors. It is worth noting that all the other expansions used in this study include enough terms so that numerical errors from these expansions are negligible compared with truncation errors in Eqs. (17a) and (17b). Therefore, truncation errors are the primary source of numerical errors, which are propagated while solving the systems of algebraic equations in Eqs. (30), (35), and (48). Other sources of error also exist; for example, solving the system of algebraic equations in Eq. (35) requires calculating the inverse matrix of the modal admittance coefficients used in Eq. (30) to obtain the matrix of modal impedance coefficients used in Eq. (35). The difference in the

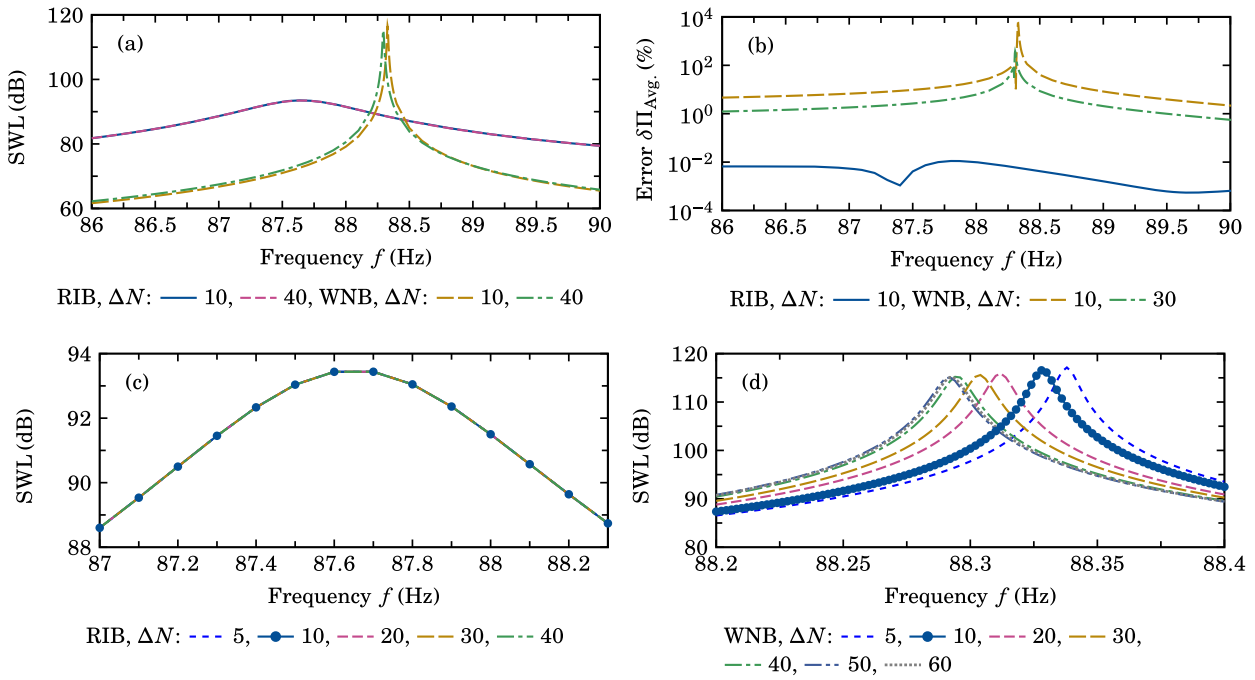


**Fig. 7.** The $\text{SWL}_{\text{Avg.}}$ for the acoustic power averaged over all 21 excitation points shown in Fig. 4 (cf. Putra and Thompson [14], Fig. 2, thin curves): (a) a wide frequency interval of $f = 86.0 \div 91.0$ Hz for $\Delta N = 10$ and the plate either in the RIB or WNB; (b) a narrow frequency interval of $f = 87.0 \div 88.3$ Hz for $\Delta N = 5, \ldots, 40$ and the plate in the RIB; (c) a very narrow frequency interval of $f = 88.2 \div 88.4$ Hz for $\Delta N = 5, \ldots, 60$ and the plate in WNB.

complex acoustic power obtained by solving the systems of equations in Eqs. (30) and (35) does not exceed $10^{-12}$ % and such errors are negligible. The effect of the MNI on the approximation error of the acoustic power averaged over 21 different excitation points as a function of $\Delta N$ with the reference values calculated for $\Delta N = 60$ is presented in Fig. 6 and (b) for arbitrarily selected frequencies. The error does not exceed a few percent for all analyzed frequencies, including 5 kHz, which is above the critical frequency $f_c = 3980.1$ Hz, regardless of whether the plate is vibrating in the RIB or WNB. The error decreases uniformly with increasing MNI for the plate in the RIB. In the case of the plate in WNB, the error decreases with increasing MNI, but the decrease occurs in steps.

In addition, the effect of the MNI on the accuracy of the numerical results obtained for the SWL of the acoustic power averaged over 21 different excitation points is presented in Fig. 7(a)–(d) within a very narrow frequency interval of 5 Hz around the resonant maxima of the fundamental mode of the vibrating plate in the RIB and WNB in Fig. 7(a). The two curves for the plate in the RIB assume values higher on average by about 20 dB than the two curves for the plate in WNB across the entire frequency interval, except at the resonant frequencies where the situation is reversed. More importantly, the two curves for the RIB are nearly identical, whereas the two curves for the WNB are slightly shifted at the resonant frequency. The shift is very small and the maxima are very steep. Consequently, this small frequency shift results in SWL variations smaller than 2 dB, yet very large percentage errors in the immediate vicinity of the resonant maximum, as illustrated in Fig. 7(b). Since the resonant maxima for the plate in WNB are extremely narrow, the large errors are of little practical importance, as are the small frequency shifts. This effect has already been discussed for a vibrating elastically supported annular plate by Rdzanek et al. [35] (cf. their Figure 6). At the same time, for the plate in the RIB, the error is smaller than 0.01 % at the resonant maximum. It can also be observed that in the RIB case, the resonant maximum is relatively wide (cf. Fig. 7(c)), while in the WNB case the resonant maximum is extremely narrow (cf. Fig. 7(d)). Virtually no effect of $\Delta N$ on the resonant curve can be seen in Fig. 7(c), as the maximum is relatively wide. On the other hand, increasing $\Delta N$ shifts the resonant maximum toward lower frequencies. Nevertheless, the shift does not exceed 0.05 Hz (0.06 %) and stabilizes at about 88.29 Hz. This shift is so small that, from a practical standpoint, it can be neglected, especially as, in the WNB case, the resonant maximum is extremely narrow. Only the lowest resonant maxima are shown in Fig. 7(a), but the behavior of higher resonant maxima is similar.

The mean square approximation error $\delta\Pi_{\text{Avg.}}$ (%) for the averaged acoustic power calculated using Eq. (72) for $\Delta N = 5, 10, 20, 30$ with the reference values calculated for $\Delta N = 40$ is presented in Table 3. In the case of the plate in the RIB, the error is about 1 % and about 3 % for the plate in WNB for $\Delta N = 10$. Such errors were considered acceptable in this study for subsequent numerical calculations. The error for the plate in WNB can be reduced by half when $\Delta N$ is increased to 30. However, in this case, the mean computation time increases by nearly an order of magnitude. The mean ratio

$$\tau = \frac{1}{\Delta f} \int_{f_1}^{f_2} \frac{t_1}{t_2} \, \mathrm{d}f, \tag{73}$$

**Table 3**
The mean square approximation error $\delta\Pi_{\text{Avg.}}$ (%) for the averaged acoustic power, calculated using Eq. (72) for $\Delta N = 5, 10, 20, 30$ with reference values obtained for $\Delta N = 40$.

| $\Delta N$ | 5 | 10 | 20 | 30 |
|---|---|---|---|---|
| Infinite Baffle | 2.827 % | 1.134 % | 0.395 % | 0.167 % |
| No Baffle | 4.038 % | 2.865 % | 2.091 % | 1.572 % |

**Table 4**
The mean ratio $\tau$ in Eq. (73) of time necessary for calculations of the averaged acoustic power $\Pi_{\text{Avg.}}$ (W) for different values of $\Delta N$ with the reference time obtained for $\Delta N = 40$.

| $\Delta N$ | 5 | 10 | 20 | 30 |
|---|---|---|---|---|
| Infinite Baffle | 0.03865 | 0.07330 | 0.2035 | 0.4981 |
| No Baffle | 0.03285 | 0.06592 | 0.1940 | 0.4891 |

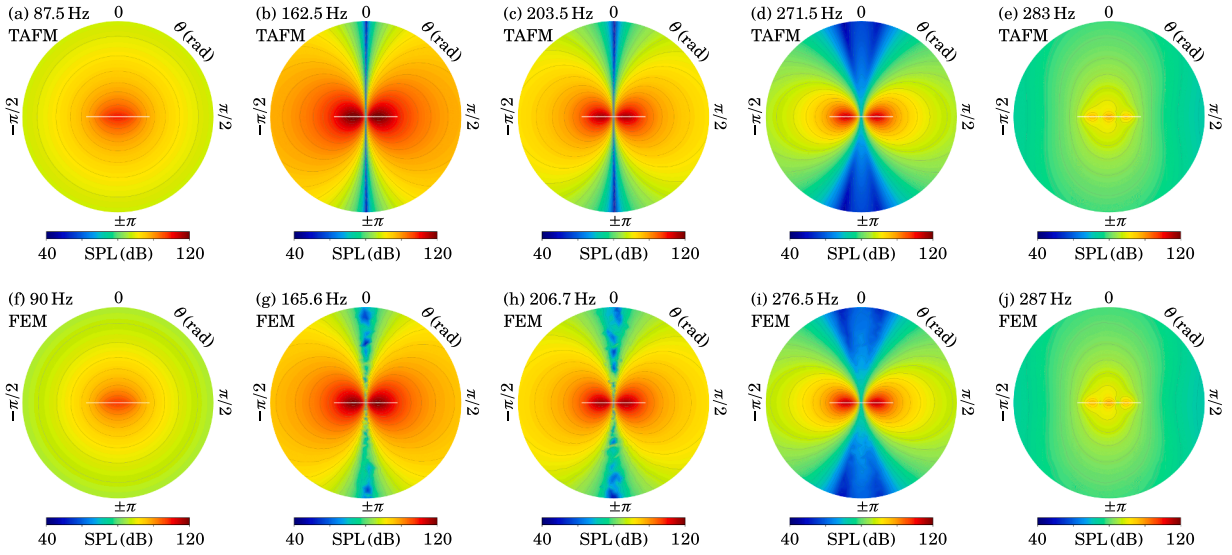


**Fig. 8.** The SPL (dB) of the vibrating plate in the RIB in the near-field for the excitation point with the coordinates $x' = 0.24a$ and $y' = 0.24b$, and the selected low frequencies as a function of $0 \leqslant |\theta| \leqslant \pi$, $\phi = \arctan(b/a)$, and $0 \leqslant r \leqslant 3r_0$, where $r_0^2 = (a/2)^2 + (b/2^2)$, calculated using: (a)–(e) the TAFM, (f)–(j) the FEM.

was averaged over the frequency interval from $f_1 = 0$ Hz to $f_2 = 10$ kHz, where $\Delta f = f_2 - f_1$. Here, $t_1$ denotes the time required to calculate the acoustic power $\Pi_{\text{Avg.}}$ (W) averaged over the 21 excitation points shown in Fig. 4 for $\Delta N = 5, 10, 20, 30$, and $t_2$ represents the reference time obtained for $\Delta N = 40$ (cf. Table 4).

This part of the numerical analysis examines the acoustic near-field and far-field using the TAFM developed in this study and validates it by comparison with the FEM. For this purpose, the sound pressure level SPL$= 10\log_{10}[|p|^2/(2p_0^2)]$ was calculated, where $|p|$ is the acoustic pressure amplitude modulus obtained from Eqs. (24) and (51), and $p_0 = 20$ μPa is the reference value. The calculations were performed for $0 \leqslant |\theta| \leqslant \pi$, $\phi = \arctan(b/a)$, and distances from the plate center $0 \leqslant r \leqslant 3r_0$, where $r_0^2 = (a/2)^2 + (b/2^2)$. The analysis focused on the lower resonant frequencies listed in Table 1 for both the plate in the RIB and the plate in WNB. Both the TAFM and FEM were applied for comparison. The specific plane $\phi = \arctan(b/a)$ was chosen to avoid cases where the acoustic field vanishes in planes parallel to the plate edges, as these coincide with nodal planes. Fig. 8 presents the SPL radiated by the plate in the RIB, and Fig. 9 shows the SPL radiated by the plate in WNB. The resonant frequencies obtained by the two methods differ slightly, but the results are highly consistent for each frequency, thus validating both approaches. In the TAFM, Eqs. (51) and (24) were employed, satisfying the homogeneous Neumann and Dirichlet boundary conditions, respectively, for $z = 0$, $|x| > a/2$, and $|y| > b/2$. Fig. 10 shows similar results for SPL at the higher resonant frequencies listed in Table 1 for the plates in both RIB and WNB. For these cases, only the TAFM was used. At the fundamental resonant frequency, the SPL exhibits a nearly omnidirectional pattern. As frequency increases, the number of side lobes grows as expected.

The SPL in the far-field as the function of the polar angle $\theta$ has been presented in Fig. 11. These results were obtained using Eqs. (24) and (51) for the resonant frequencies listed in Table 1, at a distance of $R = 10$ m from the plate center, for both theRIB and WNB cases. For the plate in the RIB, the far-field pattern in Fig. 11(a) is nearly omnidirectional at the fundamental resonant frequency

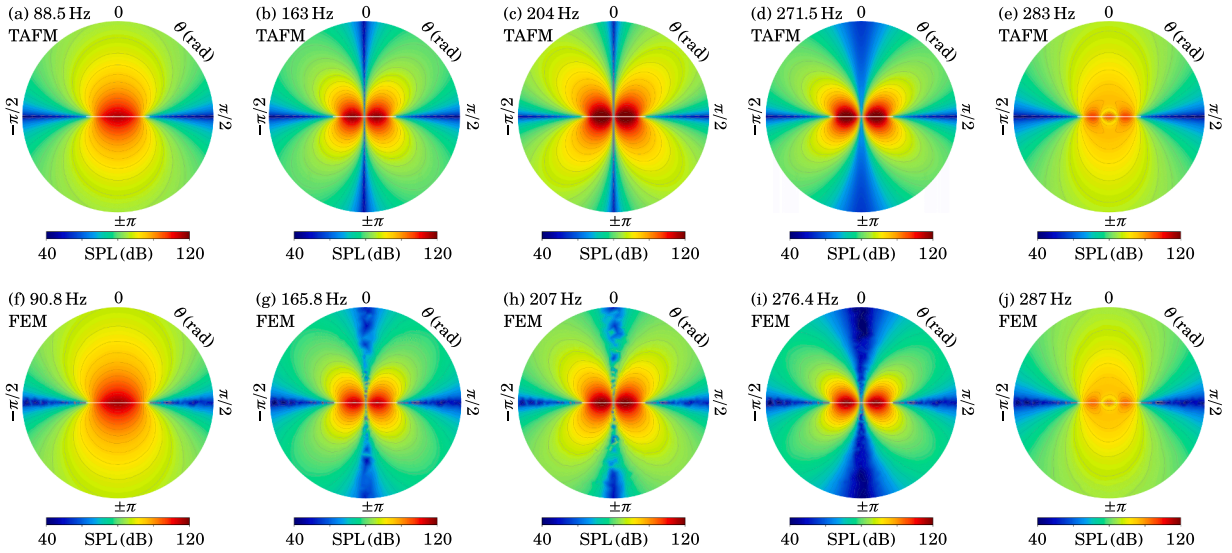


**Fig. 9.** The SPL (dB) of the vibrating plate WNB in the near-field for the excitation point with the coordinates $x' = 0.24a$ and $y' = 0.24b$, and the selected low frequencies as a function of $0 \leqslant |\theta| \leqslant \pi$, $\phi = \arctan(b/a)$, and $0 \leqslant r \leqslant 3r_0$, where $r_0^2 = (a/2)^2 + (b/2^2)$, calculated using: (a)–(e) the TAFM, (f)–(j) the FEM.

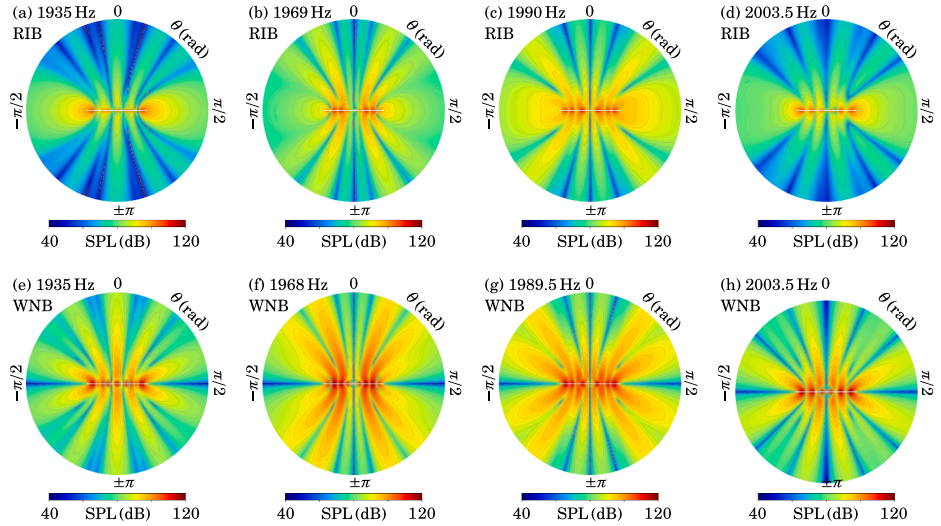


**Fig. 10.** The SPL (dB) in the near-field for the excitation point with the coordinates $x' = 0.24a$ and $y' = 0.24b$, and the selected high frequencies as a function of $0 \leqslant |\theta| \leqslant \pi$, $\phi = \arctan(b/a)$, and $0 \leqslant r \leqslant 3r_0$, where $r_0^2 = (a/2)^2 + (b/2^2)$, calculated using the formulas presented in this study for the plate vibrating: (a) in the RIB, (b) WNB.

and develops maxima at higher resonant frequencies. For the plate in WNB, the far-field pattern in Fig. 11(c) exhibits a clear horizontal nodal plane at $\theta = \pi/2$ ($z = 0$) across all resonant frequencies due to the Dirichlet boundary condition. The maximum occurs at $\theta = 0$ for the fundamental resonant frequency and shifts to $\theta \neq 0$ for higher resonant frequencies. The SPL in the far-field as a function of the azimuthal angle $\phi$, presented in Fig 11(b) and (d), is nearly omnidirectional at the fundamental resonant frequency for both RIB and WNB. At higher resonant frequencies, however, the field becomes axially asymmetric, forming vertical nodal planes at specific values of $\phi$ such as 0 and $\pi/2$, depending on the dominant mode corresponding to each resonant frequency.

The SPL in the far-field for some higher resonant frequencies is presented in Fig. 12. Generally, the SPL as a function of the polar angle $\theta$ shows a growing number of nodal lobes with increasing resonant frequency, regardless of whether the plate is in the RIB or WNB, as shown in Fig. 12(a) and (c). This indicates that the field develops a larger number of nodal cones for different values of $\theta$ as the frequency increases. The SPL in the far-field as a function of the azimuthal angle $\phi$ is shown in Fig. 12(b) and (d). It demonstrates that the number of lobes for different values of $\phi$ increases with frequency. This means that the number of vertical nodal planes also grows with frequency.

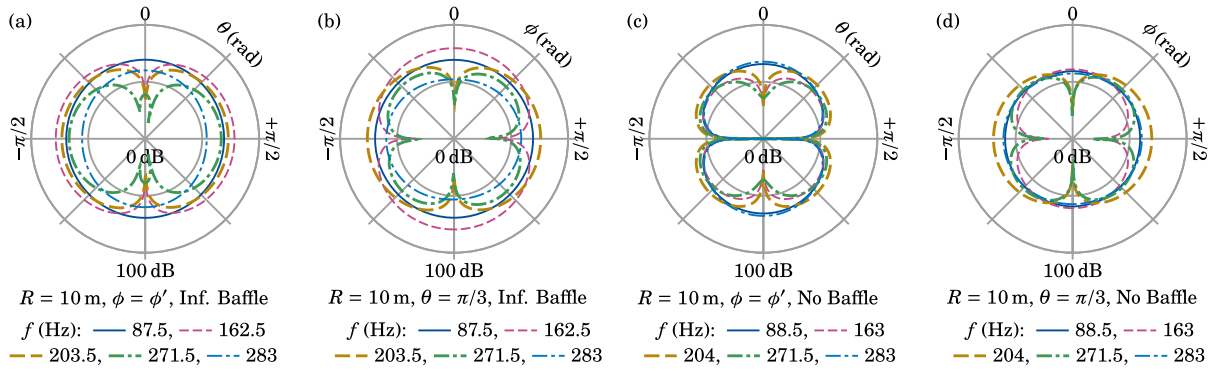


**Fig. 11.** The SPL (dB) in the far-field for $R = 10\,\mathrm{m}$, the excitation point with the coordinates $x' = 0.24a$ and $y' = 0.24b$, and the selected low frequencies as a function of: (a) $\theta$ for $\phi = \arctan(b/a)$ in the RIB, (b) $\phi$ for $\theta = \pi/3$ in the RIB, (c) $\theta$ for $\phi = \arctan(b/a)$ WNB, (d) $\phi$ for $\theta = \pi/3$ WNB.

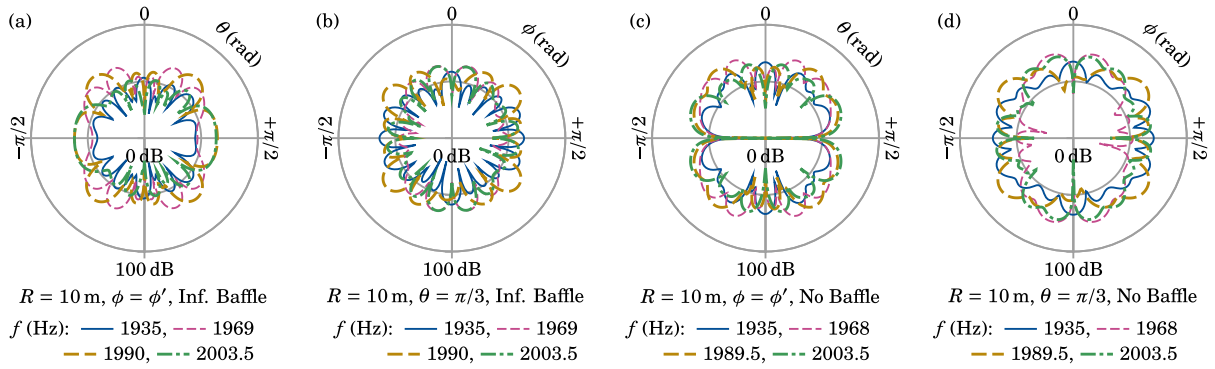


**Fig. 12.** The SPL (dB) in the far-field for $R = 10\,\mathrm{m}$, the excitation point with coordinates $x' = 0.24a$ and $y' = 0.24b$, and the selected high frequencies as a function of: (a) $\theta$ for $\phi = \arctan(b/a)$ in the RIB, (b) $\phi$ for $\theta = \pi/3$ in the RIB, (c) $\theta$ for $\phi = \arctan(b/a)$ in WNB, (d) $\phi$ for $\theta = \pi/3$ in WNB.

## 5. Conclusions

The major findings of this study are summarized below. A new rigorous analysis method, called the TAFM, has been proposed. Using this method, it is possible to effectively and accurately solve the Neumann and Dirichlet boundary problems, and analyze the acoustic field of a thin rectangular plate in the RIB and WNB, respectively. The results obtained can be useful for predicting the acoustic field of casing elements in the form of thin rectangular plates used in industrial environments. Applying the TAFM made it possible to efficiently obtain accurate numerical results for the acoustic power within a wide frequency interval, from values below the fundamental frequency of a clamped rectangular plate to far above the critical frequency. Once the modal impedance coefficients are calculated for the plate in the RIB, they can be used to efficiently calculate the complementary modal admittance coefficient for the same plate in WNB. This requires using the spectral mapping method, radial polynomials, and the Dini series for such calculations. The presented TAFM is much more robust, accurate, and efficient than both the TIFM and the FEM. For example, the TAFM makes it possible to obtain accurate results up to 10 kHz, whereas the FEM provides accurate results only up to 330 Hz. This is because the TAFM is significantly less demanding in terms of computational resources. The TAFM is approximately twice as time-efficient as the FEM when obtaining the first curve for a selected excitation point. Further curves can then be obtained in negligible time for different excitation points, while the FEM requires repeating the time-consuming calculations. This means that the TAFM remains a subject for further optimization. The NAVMI factors are useful for determining approximate values of the resonant frequencies of the plate, which agree well with the exact results as well as with those from the FEM. The results for the acoustic power obtained with the TAFM are generally consistent with those obtained using FEM. The findings confirm that the vibrating plate in WNB is a much weaker radiator than the same plate in the RIB for frequencies below the critical frequency of the plate, i.e., the radiation efficiency and acoustic power are much smaller. The TAFM makes it possible to obtain the acoustic pressure distribution both in the near-field and in the far-field. The Rayleigh first integral and the Rayleigh second integral are useful for such calculations for the plate in the RIB and the plate in WNB, respectively.

## CRediT authorship contribution statement

**Wojciech P. Rdzanek:** Writing – original draft, Visualization, Software, Methodology, Conceptualization; **Jerzy Wiciak:** Writing – original draft, Methodology, Conceptualization; **Krzysztof Szemela:** Writing – original draft, Methodology, Conceptualization; **Marek Pawelczyk:** Writing – original draft, Methodology, Conceptualization; **Li Cheng:** Writing – original draft, Methodology, Conceptualization.

## Data availability

No data was used for the research described in the article.

## Declaration of competing interest

The authors declare that they have no known competing financial interests or personal relationships that could have appeared to influence the work reported in this paper.

## Acknowledgments

The research presented in this paper was partially supported by the Center for Innovation and Transfer of Natural Sciences and Engineering Knowledge Project at the University of Rzeszów, Poland. The work was supported in part by the project IN–NOVA: "Active reduction of noise transmitted into and from enclosures through encapsulated structures," which received funding from the European Union's Horizon Europe program under the Marie Sklodowska–Curie grant agreement no. 101073037.

## Appendix A. Calculating analytically the integral in Eq. (57)

For the analytical calculation of the integral in Eq. (57), the following Graf addition theorem can be applied (cf. Olver et al. [47] Eq. 10.23.7 on p. 247),

$$J_{|m|}(\tau r)\mathrm{e}^{-\mathrm{i}|m|\phi} = \sum_{\mu=-\infty}^{+\infty}(-\mathrm{i})^{\mu}J_{|m|+\mu}(\tau x)J_{\mu}(\tau y) = \frac{1}{2}\left[J_{|m|}(\tau x)J_0(\tau y)+(-\mathrm{i})^{|m|}J_0(\tau x)J_{|m|}(\tau y)\right] + \frac{1}{2}\sum_{\mu=1}^{\infty}(-\mathrm{i})^{\mu}\left\{\left[J_{|m|+\mu}(\tau x)+J_{|m|-\mu}(\tau x)\right]J_{\mu}(\tau y)+(-1)^{\mu}(-\mathrm{i})^{|m|}J_{\mu}(\tau x)\left[J_{|m|+\mu}(\tau y)+J_{|m|-\mu}(\tau y)\right]\right\}, \tag{A.1}$$

where the substitutions are $w=\tau r$, $u=\tau y$, $v=\tau x$, $\gamma=\phi$, $\mu=m$, $k=\mu$, and $\mathrm{e}^{-\mathrm{i}\mu\pi/2}=(-\mathrm{i})^{\mu}$. When $|m|-\mu<0$ in Eq. (A.1), the following relations can be used: $J_{|m|-\mu}(\tau x)=(-1)^{|m|-\mu}J_{\mu-|m|}(\tau x)$ and $J_{|m|-\mu}(\tau y)=(-1)^{|m|-\mu}J_{\mu-|m|}(\tau y)$, which ensure that the order of the Bessel functions is always non-negative. Sufficient accuracy can be obtained in Eq. (A.1) by assuming that $|\mu|\geqslant 10+|m|$. Then, inserting Eq. (A.1) into Eq. (57) gives (note that $n$ can be used here interchangeably with $q$ and $p$ since it is the mode number $(q,p)$)

$$\hat{D}_n^{|m|}(\tau) = \frac{ab}{16\pi}\left\{\hat{D}_{|m|,q}(\xi)\tilde{\tilde{D}}_{0,p}(\zeta)+\sum_{\mu=1}^{\infty}(-\mathrm{i})^{\mu}\left[\hat{D}_{|m|+\mu,q}(\xi)+\hat{D}_{|m|-\mu,q}(\xi)\right]\tilde{\tilde{D}}_{\mu,p}(\zeta)\right\} + \frac{ab}{16\pi}(-\mathrm{i})^{|m|}\left\{\hat{D}_{0,q}(\xi)\tilde{\tilde{D}}_{|m|,p}(\zeta)+\sum_{\mu=1}^{\infty}\mathrm{i}^{\mu}\hat{D}_{\mu,q}(\xi)\left[\tilde{\tilde{D}}_{|m|+\mu,p}(\zeta)+\tilde{\tilde{D}}_{|m|-\mu,p}(\zeta)\right]\right\}, \tag{A.2}$$

since $\hat{\hat{D}}_{\mu,q}(\zeta)=(-1)^{\mu}\hat{\hat{D}}_{-\mu,q}(\zeta)$, $\tilde{\tilde{D}}_{\mu,p}(\zeta)=(-1)^{\mu}\tilde{\tilde{D}}_{-\mu,p}(\zeta)$. When $|m|-\mu<0$, the following relations can be used: $\hat{\hat{D}}_{|m|-\mu,q}(\zeta)=(-1)^{|m|-\mu}\hat{\hat{D}}_{\mu-|m|,q}(\zeta)$, and $\tilde{\tilde{D}}_{|m|-\mu,p}(\zeta)=(-1)^{|m|-\mu}\tilde{\tilde{D}}_{\mu-|m|,p}(\zeta)$. It can be obtained, by substituting $\tau x=\xi u$, $\tau y=\zeta w$, $x=ua/2$, and $y=wb/2$, that

$$\hat{\hat{D}}_{\mu,q}(\xi)=\frac{2}{a}\int_{-a/2}^{+a/2}J_{\mu}(\tau x)\Psi_q(x+a/2)\mathrm{d}x=\int_{-1}^{+1}J_{\mu}(\xi u)\hat{\hat{\psi}}_q(u)\mathrm{d}u, \tag{A.3a}$$

$$\tilde{\tilde{D}}_{\mu,p}(\zeta)=\frac{2}{b}\int_{-b/2}^{+b/2}J_{\mu}(\tau y)\Phi_p(y+b/2)\mathrm{d}y=\int_{-1}^{+1}J_{\mu}(\zeta w)\tilde{\tilde{\phi}}_p(w)\mathrm{d}w, \tag{A.3b}$$

where $\xi=\tau a/2$, $\zeta=\tau b/2$, and

$$\hat{\hat{\psi}}_q(u)=\Psi_q[(1+u)a/2], \tag{A.4a}$$

$$\tilde{\tilde{\phi}}_p(w)=\Phi_p[(1+w)b/2]. \tag{A.4b}$$

Now, taking into account that $J_{\mu}(-u)=J_{-\mu}(u)=(-1)^{\mu}J_{\mu}(u)$, $\hat{\hat{\psi}}_q(-u)=(-1)^{q+1}\hat{\hat{\psi}}_q(u)$, $\tilde{\tilde{\phi}}_p(-w)=(-1)^{p+1}\tilde{\tilde{\phi}}_p(w)$, it follows that

$$\hat{\hat{D}}_{\mu,q}(\xi)=2\int_0^1 J_{\mu}(\xi u)\hat{\hat{\psi}}_q(u)\mathrm{d}u;\quad \mu+q=1,3,\ldots, \tag{A.5a}$$

$$\tilde{\tilde{D}}_{\mu,p}(\zeta) = 2\int_0^1 J_\mu(\zeta w)\tilde{\tilde{\phi}}_p(w)\mathrm{d}w; \quad \mu+p=1,3,\ldots, \tag{A.5b}$$

with $\hat{\hat{D}}_{\mu,q}(\xi)=0$ for $\mu+q=2,4,\ldots$, and $\tilde{\tilde{D}}_{\mu,p}(\zeta)=0$ for $\mu+p=2,4,\ldots$, where

$$\hat{\hat{\psi}}_q(-u) = \Psi_q[(1-u)a/2], \qquad \hat{\hat{D}}_{\mu,q}(\xi) = (-1)^\mu \hat{\hat{D}}_{-\mu,q}(\xi), \tag{A.6a}$$

$$\tilde{\tilde{\phi}}_p(-w) = \Phi_p[(1-w)b/2], \qquad \tilde{\tilde{D}}_{\mu,p}(\zeta) = (-1)^\mu \tilde{\tilde{D}}_{-\mu,p}(\zeta). \tag{A.6b}$$

Next, the following expansion can be used (cf. Wimp [48] Eqs. (2.22) and (2.23))

$$J_\mu(\xi u) = \sum_{\mu'=0}^{\infty} \hat{\hat{D}}_{\mu,\mu'}(\xi) T_{2\mu'+\bar{\beta}(\mu)}(u), \tag{A.7a}$$

$$J_\mu(\zeta w) = \sum_{\mu'=0}^{\infty} \hat{\hat{D}}_{\mu,\mu'}(\zeta) T_{2\mu'+\bar{\beta}(\mu)}(w), \tag{A.7b}$$

where $T_n(u)$ stands for the Chebyshev polynomials of the first kind (cf. Abramowitz and Stegun [38] Eq. 22.2.4 p. 774), the integer part and the rest of dividing an integer value $\mu$ by 2 are $\bar{\alpha}(\mu)=\mathrm{Integer}(\mu/2)$ and $\bar{\beta}(\mu)=\mathrm{Rest}(\mu/2)$, and

$$\hat{\hat{D}}_{\mu,\mu'}(\xi) = \mathrm{i}^{|\mu|-\mu}\epsilon_{\bar{\beta}(|\mu|)+\mu'} J_{\lceil|\mu|/2\rceil+\mu'}(\xi/2) J_{\bar{\alpha}(|\mu|)-\mu'}(\xi/2), \tag{A.8}$$

$\epsilon_0=1$ and $\epsilon_{\mu'}=2$ for $\mu'\neq 0$, $\mathrm{i}^{|\mu|-\mu}=1$ for $\mu=0,1,.,$ $\mathrm{i}^{|\mu|-\mu}=(-1)^\mu$ for $\mu=-1,-2,.,$ and $\lceil|\mu|/2\rceil=\bar{\alpha}(|\mu|)+\bar{\beta}(|\mu|)$ ($\lceil x\rceil$ is the smallest integer greater equal $x$). It is convenient to apply the expansion in Eqs. (A.7a) and (A.7b) as it separates variables $\xi$ and $u$. Then $T$ polynomials are orthogonal on the interval of $u$ from $-1$ do $+1$ exactly as the normalized coordinates $x/x_0$ and $y/y_0$ on the plate. Also, $\xi=\tau a/2$ and $\zeta=\tau b/2$ assume values from 0 to $\infty$ as they are the normalized wavenumbers. A sufficient accuracy can be obtained in Eqs. (A.7a) and (A.7b) by assuming that all terms are included for $\mu'$ from 0 to minimum $10+\lceil\xi/2\rceil$ ($\leqslant 11+\mathrm{Integer}(\xi/2)$). Applying the expansion in Eqs. (A.7a) and (A.7b) to Eqs. (A.3a) and (A.3b) gives

$$\hat{\hat{D}}_{\mu,q}(\xi) = \sum_{\mu'=0}^{\infty} \hat{T}_{2\mu'+\bar{\beta}(\mu),q}\hat{\hat{D}}_{\mu,\mu'}(\xi), \tag{A.9a}$$

$$\tilde{\tilde{D}}_{\mu,p}(\zeta) = \sum_{\mu'=0}^{\infty} \tilde{T}_{2\mu'+\bar{\beta}(\mu),p}\hat{\hat{D}}_{\mu,\mu'}(\zeta), \tag{A.9b}$$

for odd $\mu+q$ and $\mu+p$ and zero otherwise, where

$$\hat{T}_{\mu,q} = \int_{-1}^{+1} T_\mu(u)\hat{\hat{\psi}}_q(u)\mathrm{d}u = 2\int_0^1 T_\mu(u)\hat{\hat{\psi}}_q(u)\mathrm{d}u; \quad \mu+q=1,3,\ldots, \tag{A.10a}$$

$$\tilde{T}_{\mu,p} = \int_{-1}^{+1} T_\mu(w)\tilde{\tilde{\phi}}_p(w)\mathrm{d}w = 2\int_0^1 T_\mu(w)\tilde{\tilde{\phi}}_p(w)\mathrm{d}w; \quad \mu+p=1,3,\ldots, \tag{A.10b}$$

$\hat{T}_{\mu,q}=0$ for $\mu+q=2,4,\ldots$, $\tilde{T}_{\mu,p}=0$ for $\mu+p=2,4,\ldots$, by substituting $\mu$ for $2\mu'+\bar{\beta}(\mu)$, and $n$ for $q$ and $p$ as $n\equiv(q,p)$, since $T_\mu(-u)=(-1)^\mu T_\mu(u)$, and $T_\mu(-w)=(-1)^\mu T_\mu(w)$.

The integrals in Eqs. (A.10a) and (A.10b) can be calculated as follows

$$\hat{T}_{\mu,q} = A_{1,q}\left(\hat{T}_{1,\mu,q} - \bar{k}_{1,q}\frac{\alpha_{2,q}}{\alpha_{1,q}}\hat{T}_{2,\mu,q} - \hat{T}_{3,\mu,q} + \bar{k}_{1,q}\hat{T}_{4,\mu,q}\right), \tag{A.11a}$$

$$\tilde{T}_{\mu,p} = A_{2,p}\left(\tilde{T}_{1,\mu,p} - \bar{k}_{2,p}\frac{\beta_{2,p}}{\beta_{1,p}}\tilde{T}_{2,\mu,p} - \tilde{T}_{3,\mu,p} + \bar{k}_{2,p}\tilde{T}_{4,\mu,p}\right), \tag{A.11b}$$

where

$$\hat{T}_{1,\mu,q} = \int_{-1}^{+1} T_\mu(u)\cos[(1+u)\alpha_{1,q}a/2]\mathrm{d}u = \hat{T}^{(c)}_{1,\mu,q}\cos(\alpha_{1,q}a/2) - \hat{T}^{(s)}_{1,\mu,q}\sin(\alpha_{1,q}a/2), \tag{A.12a}$$

$$\hat{T}_{2,\mu,q} = \int_{-1}^{+1} T_\mu(u)\sin[(1+u)\alpha_{1,q}a/2]\mathrm{d}u = \hat{T}^{(c)}_{1,\mu,q}\sin(\alpha_{1,q}a/2) + \hat{T}^{(s)}_{1,\mu,q}\cos(\alpha_{1,q}a/2), \tag{A.12b}$$

$$\begin{aligned}\hat{T}_{3,\mu,q} &= \int_{-1}^{+1} T_\mu(u)\cosh[(1+u)\alpha_{2,q}a/2]\mathrm{d}u = \hat{T}^{(ch)}_{1,\mu,q}\cosh(\alpha_{2,q}a/2) + \hat{T}^{(sh)}_{1,\mu,q}\sinh(\alpha_{2,q}a/2)\\ &= \mathrm{e}^{\alpha_{2,q}a/2}\hat{T}^{(+)}_{1,\mu,q} + \mathrm{e}^{-\alpha_{2,q}a/2}\hat{T}^{(-)}_{1,\mu,q} = \mathrm{e}^{\alpha_{2,q}a/2}\sum_{r=0}^{\mu}\tilde{\alpha}_{\mu,r}i^{(1)}_r(\alpha_{2,q}a/2) + \mathrm{e}^{-\alpha_{2,q}a/2}\sum_{r=0}^{\mu}\tilde{\alpha}_{\mu,r}(-1)^r i^{(1)}_r(\alpha_{2,q}a/2),\end{aligned} \tag{A.12c}$$

$$\hat{T}_{4,\mu,q} = \int_{-1}^{+1} T_\mu(u)\sinh[(1+u)\alpha_{2,q}a/2]\mathrm{d}u = \hat{T}^{(ch)}_{1,\mu,q}\sinh(\alpha_{2,q}a/2) + \hat{T}^{(sh)}_{1,\mu,q}\cosh(\alpha_{2,q}a/2)$$

$$= \mathrm{e}^{\alpha_{2,q}a/2}\hat{T}^{(+)}_{1,\mu,q} - \mathrm{e}^{-\alpha_{2,q}a/2}\hat{T}^{(-)}_{1,\mu,q} = \mathrm{e}^{\alpha_{2,q}a/2}\sum_{r=0}^{\mu}\tilde{\alpha}_{\mu,r}i_r^{(1)}(\alpha_{2,q}a/2) - \mathrm{e}^{-\alpha_{2,q}a/2}\sum_{r=0}^{\mu}\tilde{\alpha}_{\mu,r}(-1)^r i_r^{(1)}(\alpha_{2,q}a/2), \tag{A.12d}$$

$$\hat{T}^{(+)}_{1,\mu,q} = \frac{1}{2}\int_{-1}^{+1} T_\mu(u)\mathrm{e}^{u\alpha_{2,q}a/2}\mathrm{d}u = \sum_{r=0}^{\mu}\tilde{\alpha}_{\mu,r}\frac{1}{2}\int_{-1}^{+1}\mathrm{e}^{u\alpha_{2,q}a/2}P_r(u)\mathrm{d}u = \sum_{r=0}^{\mu}\tilde{\alpha}_{\mu,r}i_r^{(1)}(\alpha_{2,q}a/2), \tag{A.12e}$$

$$\hat{T}^{(-)}_{1,\mu,q} = \frac{1}{2}\int_{-1}^{+1} T_\mu(u)\mathrm{e}^{-u\alpha_{2,q}a/2}\mathrm{d}u = \sum_{r=0}^{\mu}\tilde{\alpha}_{\mu,r}\frac{1}{2}\int_{-1}^{+1}\mathrm{e}^{-u\alpha_{2,q}a/2}P_r(u)\mathrm{d}u = \sum_{r=0}^{\mu}\tilde{\alpha}_{\mu,r}(-1)^r i_r^{(1)}(\alpha_{2,q}a/2), \tag{A.12f}$$

$$\frac{1}{2}\int_{-1}^{+1}\mathrm{e}^{u\alpha_{2,q}a/2}P_r(u)\mathrm{d}u = i_r^{(1)}(\alpha_{2,q}a/2), \tag{A.12g}$$

$$\frac{1}{2}\int_{-1}^{+1}\mathrm{e}^{-u\alpha_{2,q}a/2}P_r(u)\mathrm{d}u = (-1)^r i_r^{(1)}(\alpha_{2,q}a/2), \tag{A.12h}$$

$$\frac{1}{2}\int_{-1}^{+1}\mathrm{e}^{\pm ua}P_n(u)\mathrm{d}u = (\pm 1)^n i_n^{(1)}(a), \tag{A.12i}$$

$$\tilde{T}_{1,\mu,p} = \int_{-1}^{+1} T_\mu(w)\cos[(1+w)\beta_{1,p}b/2]\mathrm{d}w = \tilde{T}^{(c)}_{2,\mu,p}\cos(\beta_{1,p}b/2) - \tilde{T}^{(s)}_{2,\mu,p}\sin(\beta_{1,p}b/2), \tag{A.12j}$$

$$\tilde{T}_{2,\mu,p} = \int_{-1}^{+1} T_\mu(w)\sin[(1+w)\beta_{1,p}b/2]\mathrm{d}w = \tilde{T}^{(c)}_{2,\mu,p}\sin(\beta_{1,p}b/2) + \tilde{T}^{(s)}_{2,\mu,p}\cos(\beta_{1,p}b/2), \tag{A.12k}$$

$$\tilde{T}_{3,\mu,p} = \int_{-1}^{+1} T_\mu(w)\cosh[(1+w)\beta_{2,p}b/2]\mathrm{d}w = \tilde{T}^{(ch)}_{2,\mu,p}\cosh(\beta_{2,p}b/2) + \tilde{T}^{(sh)}_{2,\mu,p}\sinh(\beta_{2,p}b/2), \tag{A.12l}$$

$$\tilde{T}_{4,\mu,p} = \int_{-1}^{+1} T_\mu(w)\sinh[(1+w)\beta_{2,p}b/2]\mathrm{d}w = \tilde{T}^{(ch)}_{2,\mu,p}\sinh(\beta_{2,p}b/2) + \tilde{T}^{(sh)}_{2,\mu,p}\cosh(\beta_{2,p}b/2), \tag{A.12m}$$

since $i_n^{(1)}(-a) = (-1)^n i_n^{(1)}(a)$, $\cos[(1+u)\alpha_{1,q}a/2] = [\cos(\alpha_{1,q}a/2)\cos(u\alpha_{1,q}a/2) - \sin(\alpha_{1,q}a/2)\sin(u\alpha_{1,q}a/2)]$, and $\sin[(1+u)\alpha_{1,q}a/2] = [\sin(\alpha_{1,q}a/2)\cos(u\alpha_{1,q}a/2) + \cos(\alpha_{1,q}a/2)\sin(u\alpha_{1,q}a/2)]$,

$$\hat{T}^{(c)}_{1,\mu,q} = \int_{-1}^{+1} T_\mu(u)\cos(u\alpha_{1,q}a/2)\mathrm{d}u;\ \text{for even } \mu \text{ zero otherwise}, \tag{A.13a}$$

$$\hat{T}^{(s)}_{1,\mu,q} = \int_{-1}^{+1} T_\mu(u)\sin(u\alpha_{1,q}a/2)\mathrm{d}u;\ \text{for odd } \mu \text{ zero otherwise}, \tag{A.13b}$$

$$\hat{T}^{(ch)}_{1,\mu,q} = \int_{-1}^{+1} T_\mu(u)\cosh(u\alpha_{2,q}a/2)\mathrm{d}u;\ \text{for even } \mu \text{ zero otherwise}, \tag{A.13c}$$

$$\hat{T}^{(sh)}_{1,\mu,q} = \int_{-1}^{+1} T_\mu(u)\sinh(u\alpha_{2,q}a/2)\mathrm{d}u;\ \text{for odd } \mu \text{ zero otherwise}, \tag{A.13d}$$

$$\tilde{T}^{(c)}_{2,\mu,p} = \int_{-1}^{+1} T_\mu(w)\cos(w\beta_{1,p}b/2)\mathrm{d}w;\ \text{for even } \mu \text{ zero otherwise}, \tag{A.13e}$$

$$\tilde{T}^{(s)}_{2,\mu,p} = \int_{-1}^{+1} T_\mu(w)\sin(w\beta_{1,p}b/2)\mathrm{d}w;\ \text{for odd } \mu \text{ zero otherwise}, \tag{A.13f}$$

$$\tilde{T}^{(ch)}_{2,\mu,p} = \int_{-1}^{+1} T_\mu(w)\cosh(w\beta_{2,p}b/2)\mathrm{d}w;\ \text{for even } \mu \text{ zero otherwise}, \tag{A.13g}$$

$$\tilde{T}^{(sh)}_{2,\mu,p} = \int_{-1}^{+1} T_\mu(w)\sinh(w\beta_{2,p}b/2)\mathrm{d}w;\ \text{for odd } \mu \text{ zero otherwise}, \tag{A.13h}$$

since $\cosh(u\alpha_{2,q}a/2) = \cos(\mathrm{i}u\alpha_{2,q}a/2)$, and $\sinh(u\alpha_{2,q}a/2) = (-\mathrm{i})\sin(\mathrm{i}u\alpha_{2,q}a/2)$. Let us now express the Chebyshev polynomial in terms of the finite series of the Legendre polynomials as follows

$$T_\mu(x) = \sum_{r=0}^{\mu}\tilde{\alpha}_{\mu,r}P_r(x), \tag{A.14}$$

where $\tilde{\alpha}_{0,r} = \delta_{0,r}$,

$$\tilde{\alpha}_{\mu,r} = \frac{2r+1}{2}\int_{-1}^{+1} T_\mu(x)P_r(x)\mathrm{d}x, \tag{A.15}$$

for $0 \leqslant r \leqslant \mu$, $r = 0, 1, \ldots$, and the orthogonality relation has been used

$$\int_{-1}^{+1} P_r(x) P_{r'}(x) \mathrm{d}x = \frac{2}{2r+1} \delta_{rr'}. \tag{A.16}$$

Then, applying the substitution $x = \cos\theta$ to the integral in Eq. (A.15) gives

$$\tilde{\alpha}_{\mu,r} = \frac{2r+1}{2} \int_0^{\pi} T_\mu(\cos\theta) P_r(\cos\theta) \sin\theta \, \mathrm{d}\theta. \tag{A.17}$$

Now, the Legendre function can be expressed in terms of the Fourier series as follows

$$P_r(\cos\theta) = \sum_{k=0}^{\lfloor r/2 \rfloor} \epsilon_{r-2k} \tilde{\beta}_{r,k} T_{r-2k}(\cos\theta), \tag{A.18}$$

where $\lfloor x \rfloor$ is the greatest integer less than or equal to $x$, $\epsilon_0 = 1$, $\epsilon_k = 2$ for $|k| = 1, 2, \ldots$, and

$$\tilde{\beta}_{r,k} = \frac{1}{\pi} \frac{\Gamma(k+1/2)}{\Gamma(k+1)} \frac{\Gamma(r-k+1/2)}{\Gamma(r-k+1)}. \tag{A.19}$$

Subsequently, applying the series in Eq. (A.18) to the integral in Eq. (A.17) gives

$$\tilde{\alpha}_{\mu,r} = \frac{2r+1}{2} \sum_{k=0}^{\lfloor r/2 \rfloor} \epsilon_{r-2k} \tilde{\beta}_{r,k} \tilde{\gamma}_{\mu,r-2k}, \tag{A.20}$$

where

$$\tilde{\gamma}_{\mu,\nu} = \int_0^{\pi} T_\mu(\cos\theta) T_\nu(\cos\theta) \sin\theta \, \mathrm{d}\theta = \int_{-1}^{+1} T_\mu(x) T_\nu(x) \mathrm{d}x. \tag{A.21}$$

Then, applying the following relation

$$T_\mu(x) T_\nu(x) = \frac{1}{2} T_{\mu+\nu}(x) + \frac{1}{2} T_{|\mu-\nu|}(x), \tag{A.22}$$

valid for $\mu, \nu \geqslant 0$, gives

$$\tilde{\gamma}_{\mu,\nu} = \tilde{\xi}_{\mu+\nu} + \tilde{\xi}_{|\mu-\nu|}, \tag{A.23}$$

where

$$\tilde{\xi}_n = \frac{1}{2} \int_{-1}^{+1} T_n(x) \mathrm{d}x = \begin{cases} 0; & n = 1, 3, 5, \ldots, \\ (1-n^2)^{-1}; & n = 0, 2, 4, \ldots. \end{cases} \tag{A.24}$$

Then, the following relation can be employed (cf. also Gradshteyn and Ryzhik [49] Eq. (7.243.5) p. 792)

$$\int_{-1}^{+1} \mathrm{e}^{\mathrm{i}ua} P_n(u) \mathrm{d}u = 2\mathrm{i}^n j_n(a), \tag{A.25a}$$

$$\int_{-1}^{+1} \mathrm{e}^{-\mathrm{i}ua} P_n(u) \mathrm{d}u = 2(-\mathrm{i})^n j_n(a), \tag{A.25b}$$

for $a > 0$, where the spherical Bessel function is $j_n(a) = [\pi/(2a)]^{1/2} J_{n+1/2}(a)$ (cf. Abramowitz and Stegun [38] Eq. 10.1.1 p. 437). Comparing the real and imaginary parts on both sides of Eq. (A.12g) gives

$$\int_{-1}^{+1} P_{2n}(u) \sin(ua) \mathrm{d}u = 0, \tag{A.26a}$$

$$\int_{-1}^{+1} P_{2n+1}(u) \cos(ua) \mathrm{d}u = 0, \tag{A.26b}$$

$$\int_{-1}^{+1} P_{2n}(u) \cos(ua) \mathrm{d}u = 2(-1)^n j_{2n}(a), \tag{A.26c}$$

$$\int_{-1}^{+1} P_{2n+1}(u) \sin(ua) \mathrm{d}u = 2(-1)^n j_{2n+1}(a). \tag{A.26d}$$

Then

$$\hat{T}^{(c)}_{1,\mu,q} = 2 \sum_{r=0}^{\lfloor \mu/2 \rfloor} \tilde{\alpha}_{\mu,2r} (-1)^r j_{2r}(\alpha_{1,q} a/2), \tag{A.27a}$$

$$\hat{T}^{(s)}_{1,\mu,q} = 2 \sum_{r=0}^{\lfloor \mu/2 \rfloor} \tilde{\alpha}_{\mu,2r+1} (-1)^r j_{2r+1}(\alpha_{1,q} a/2), \tag{A.27b}$$

$$\hat{T}^{(ch)}_{1,\mu,q} = 2\sum_{r=0}^{\lfloor \mu/2 \rfloor} \tilde{\alpha}_{\mu,2r} i^{(1)}_{2r}(\alpha_{2,q} a/2), \tag{A.27c}$$

$$\hat{T}^{(sh)}_{1,\mu,q} = 2\sum_{r=0}^{\lfloor \mu/2 \rfloor} \tilde{\alpha}_{\mu,2r+1} i^{(1)}_{2r+1}(\alpha_{2,q} a/2), \tag{A.27d}$$

$$\tilde{T}^{(c)}_{2,\mu,p} = 2\sum_{r=0}^{\lfloor \mu/2 \rfloor} \tilde{\alpha}_{\mu,2r} (-1)^r j_{2r}(\beta_{1,p} b/2), \tag{A.27e}$$

$$\tilde{T}^{(s)}_{2,\mu,p} = 2\sum_{r=0}^{\lfloor \mu/2 \rfloor} \tilde{\alpha}_{\mu,2r+1} (-1)^r j_{2r+1}(\beta_{1,p} b/2), \tag{A.27f}$$

$$\tilde{T}^{(ch)}_{2,\mu,p} = 2\sum_{r=0}^{\lfloor \mu/2 \rfloor} \tilde{\alpha}_{\mu,2r} i^{(1)}_{2r}(\beta_{2,p} b/2), \tag{A.27g}$$

$$\tilde{T}^{(sh)}_{2,\mu,p} = 2\sum_{r=0}^{\lfloor \mu/2 \rfloor} \tilde{\alpha}_{\mu,2r+1} i^{(1)}_{2r+1}(\beta_{2,p} b/2), \tag{A.27h}$$

since $j_n(\mathrm{i}z) = \mathrm{i}^n i^{(1)}_n(z)$, where the modified Bessel function of the fractional order is $i^{(1)}_n(z) = [\pi/(2z)]^{1/2} I_{n+1/2}(z)$ (cf. Olver et al. [47] Eq. 10.47.7 on p. 262). Further substituting relations in Eqs. (A.27a)–(A.27h) to Eqs. (A.12a)–(A.12h) gives Eqs. (66a)–(66b).

In the specific case when $\mu = 0$, $T_0(u) = 1$ and, consequently (cf. Eqs. (A.10a) and (A.10b)),

$$\hat{T}_{0,q} = \int_{-1}^{+1} \hat{\psi}_q(u)\mathrm{d}u = 2\int_0^1 \hat{\psi}_q(u)\mathrm{d}u = 2\int_{-1}^0 \hat{\psi}_q(u)\mathrm{d}u; \quad q = 1,3,\ldots, \tag{A.28a}$$

$$\tilde{T}_{0,p} = \int_{-1}^{+1} \tilde{\tilde{\phi}}_p(w)\mathrm{d}w = 2\int_0^1 \tilde{\tilde{\phi}}_p(w)\mathrm{d}w = 2\int_{-1}^0 \tilde{\tilde{\phi}}_p(w)\mathrm{d}w; \quad p = 1,3,\ldots, \tag{A.28b}$$

with $\hat{T}_{0,q} = 0$ for $q = 2,4,\ldots$, and $\tilde{T}_{0,p} = 0$ for $p = 2,4,\ldots$. Further, based on Eqs. (A.4a) and (A.4b), it holds

$$\hat{T}_{0,q} = 2\int_{-1}^0 \Psi_q[(1+u)a/2]\mathrm{d}u = \frac{4}{a}\int_0^{a/2} \Psi_q(x)\mathrm{d}x; \quad q = 1,3,\ldots, \tag{A.29a}$$

$$\tilde{T}_{0,p} = 2\int_{-1}^0 \Phi_p[(1+w)b/2]\mathrm{d}w = \frac{4}{b}\int_0^{b/2} \Phi_p(y)\mathrm{d}y; \quad p = 1,3,\ldots, \tag{A.29b}$$

by substituting $(1+u)a/2 = x$ and $(1+w)b/2 = y$. Now, applying Eqs. (3b) and (3c) leads to the results presented in Eqs. (68a)–(68b).

## Appendix B. Sample rigorous manipulations

The integral in Eq. (21) can be split into the integrals for the upper and the lower surfaces of the plate as follows

$$\begin{aligned} p(\vec{r}) = &\lim_{\epsilon\to 0}\int_{S'_+}\left[\frac{\partial G(\vec{r},\vec{r}\,')}{\partial z'}p(\vec{r}\,') - \frac{\partial p(\vec{r}\,')}{\partial z'}G(\vec{r},\vec{r}\,')\right]_{z'=+\epsilon}\mathrm{d}S'_+ \\ &- \lim_{\epsilon\to 0}\int_{S'_-}\left[\frac{\partial G(\vec{r},\vec{r}\,')}{\partial z'}p(\vec{r}\,') - \frac{\partial p(\vec{r}\,')}{\partial z'}G(\vec{r},\vec{r}\,')\right]_{z'=-\epsilon}\mathrm{d}S'_-, \end{aligned} \tag{B.1}$$

where $z' = +\epsilon$ refers to the upper surface of the plate and $z' = -\epsilon$ denotes to the lower surface of the plate for $\epsilon \to 0$, $S'_+$ represents the upper surface of the plate, and $S'_-$ is the lower surface of the plate. The derivative of the Green function, for $\epsilon \to 0$, is (cf. Eq. (22))

$$\lim_{\epsilon\to 0}\left[\frac{\partial G(\vec{r},\vec{r}\,')}{\partial z'}\right]_{z'=\pm\epsilon} = -\mathrm{i}k_0\left\{\left(1 - \frac{1}{\mathrm{i}k_0 R}\right)\frac{\mathrm{e}^{\mathrm{i}k_0 R}}{4\pi R}\,\frac{z}{R}\right\}_{z'=0}, \tag{B.2}$$

where $R = |\vec{R}| = [(x-x')^2 + (y-y')^2 + (z-z')^2]^{1/2}$. Next, applying Eq. (15) (after replacing $z$ by $z'$) gives

$$\begin{aligned} p(\vec{r}) = &\lim_{\epsilon\to 0}\int_{S'_+}\left[\frac{\partial G(\vec{r},\vec{r}\,')}{\partial z'}p(\vec{r}\,') - \mathrm{i}\omega\varrho_0 v(x+a/2, y+b/2)G(\vec{r},\vec{r}\,')\right]_{z'=+\epsilon}\mathrm{d}S'_+ \\ &- \lim_{\epsilon\to 0}\int_{S'_-}\left[\frac{\partial G(\vec{r},\vec{r}\,')}{\partial z'}p(\vec{r}\,') - \mathrm{i}\omega\varrho_0 v(x+a/2, y+b/2)G(\vec{r},\vec{r}\,')\right]_{z'=-\epsilon}\mathrm{d}S'_-. \end{aligned} \tag{B.3}$$

Now based on Eqs. (22) and (B.2), it can be noted that for $z' = 0$ and $z \geqslant 0$, it holds

$$\lim_{\epsilon\to 0}\left[G(\vec{r},\vec{r}\,')\right]_{z'=+\epsilon} = \lim_{\epsilon\to 0}\left[G(\vec{r},\vec{r}\,')\right]_{z'=-\epsilon} = G(\vec{r},\vec{r}\,')\Big|_{z'=0}, \tag{B.4a}$$

$$\lim_{\epsilon\to 0}\left[\frac{\partial G(\vec{r},\vec{r}\,')}{\partial z'}\right]_{z'=+\epsilon} = \lim_{\epsilon\to 0}\left[\frac{\partial G(\vec{r},\vec{r}\,')}{\partial z'}\right]_{z'=-\epsilon} = \frac{\partial G(\vec{r},\vec{r}\,')}{\partial z'}\Big|_{z'=0}. \tag{B.4b}$$

In addition, based on the anti-symmetry condition $p(x', y', z') = -p(x', y', -z')$, it holds

$$\lim_{\epsilon\to 0}\left[p(\vec{r}\,')\right]_{z'=+\epsilon} = -\lim_{\epsilon\to 0}\left[p(\vec{r}\,')\right]_{z'=-\epsilon} = \left[p_+(\vec{r}\,')\right]_{z'=0} = -\left[p_-(\vec{r}\,')\right]_{z'=0}, \tag{B.5}$$

where $p_+(\vec{r}\,')$ is the acoustic pressure amplitude on the upper surface of the plate and $p_-(\vec{r}\,')$ is the acoustic pressure amplitude on the lower surface of the plate.

Now, based on Eqs. (B.4a) and (B.4b), the two terms containing the Green function in Eq. (B.3) cancel each other, while the two terms containing the derivative of the Green function sum up. This results in the acoustic pressure amplitude, for $z \geqslant 0$, in the form of

$$p(\vec{r}) = \int_{S'}\left[p_+(\vec{r}\,') - p_-(\vec{r}\,')\right]_{z'=0}\frac{\partial G(\vec{r},\vec{r}\,')}{\partial z'}\bigg|_{z'=0}\mathrm{d}S', \tag{B.6}$$

where $S' = S'_+ = S'_-$ as both sides of the plate have the same surface area. Further, from Eq. (B.5) it results that the acoustic pressure difference on the plate is equal to the doubled acoustic pressure $2p(x', y', 0)$ on the upper side of the plate, which can be expressed as follows

$$\left[p_+(\vec{r}\,') - p_-(\vec{r}\,')\right]_{z'=0} = \left[2p_+(\vec{r}\,')\right]_{z'=0} = -\left[2p_-(\vec{r}\,')\right]_{z'=0} = 2p(x', y', 0). \tag{B.7}$$

Then, applying Eq. (B.7) to Eq. (B.6) yields the acoustic pressure amplitude in the form presented in Eq. (24).

## Appendix C. The approximate resonant frequencies using the NAVMI factors

In the case when $\varrho_0 \ll \varrho$ ($e_f \to 0$), the approximate resonant frequencies can be obtained by applying the procedure described by Fahy and Gardonio [32] (cf. their Eqs. (4.56)– (4.58)). For this purpose, all the terms for $n' \neq n$ have been neglected in Eq. (35) assuming that close to the $n$th resonant frequency, only the $n$th mode contributes significantly and, therefore, is dominant. Consequently, Eq. (35) is written as

$$c'_n Dk_n^4 - c'_n\omega'^2\varrho h - c'_n \mathrm{i}\varkappa\omega'^2\varrho h\hat{\lambda}_{nn} = \hat{P}_n \tag{C.1a}$$

$$c''_n Dk_n^4 - c''_n\omega''^2\varrho h = \hat{P}_n \tag{C.1b}$$

where $\omega'$ and $\omega''$ are the resonant frequencies of the plate in fluid and in vacuum, respectively, as, in addition, the fluid loading effect has been neglected in Eq. (C.1b). Similarly, $c'_n$ and $c''_n$ are valid in these two different cases. Note, that the right sides of both equations are identical and can be eliminated giving

$$c'_n Dk_n^4 - c'_n\omega'^2\varrho h - c'_n \mathrm{i}\varkappa\omega'^2\varrho h\hat{\lambda}_{nn} = c''_n Dk_n^4 - c''_n\omega''^2\varrho h \tag{C.2}$$

Now, assuming that $c'_n \approx c''_n$ and taking now the real component of the above equation gives the approximate resonant angular frequency in Eq. (46).

## Appendix D. The spectral mapping for the impedance coefficients

The following expansion series is valid for $-a/2 \leqslant x \leqslant +a/2$ and $-b/2 \leqslant y \leqslant +b/2$

$$W_n(x + a/2, y + b/2) = \sum_{\nu=0}^{\infty}\sum_{m=-\infty}^{\infty}\hat{D}_n^m(\gamma_\nu^{|m|})\bar{N}_\nu^{|m|}J_{|m|}(\gamma_\nu^{|m|}r)\mathrm{e}^{\mathrm{i}m\phi}, \tag{D.1}$$

where $x = r\cos\phi$, $y = r\sin\phi$. Applying this expansion to Eq. (7a) gives yet another expansion series

$$\bar{W}_n(k_x, k_y) = \sum_{\nu=0}^{\infty}\sum_{m=-\infty}^{\infty}(-\mathrm{i})^{|m|}\hat{D}_n^m(\gamma_\nu^{|m|})\bar{N}_\nu^{|m|}\bar{D}_\nu^{|m|}(\tau)\mathrm{e}^{+\mathrm{i}m\beta}, \tag{D.2}$$

where $k_x = \tau\cos\beta$, $k_y = \tau\sin\beta$. Now, inserting Eq. (D.2) to (32) and rearranging yields the expansion presented in Eq. (56).

## Appendix E. The TAFM numerical calculations scheme

The TAFM numerical calculations scheme is presented in Fig. E.13, where the blocks can be described as follows:

- "Eigenfrequencies": The procedure begins with determining the eigenfrequencies from the system of five characteristic equations in Eqs. (6a), (6b), and the accompanying text. The eigenfrequencies are then arranged in ascending order.
- "Truncation Condition": Next, the truncation condition $N$ in the modal expansions in Eqs. (17a) and (17b) is applied for each excitation frequency $f$, where $n = 0, \ldots, N-1$.
- "Modal Admittance": It is then decided whether the matrix of modal admittances will be calculated by direct numerical integration or by successive spectral mappings.
- "Numerical Integration": If direct numerical integration is selected, the $N \times N$ admittance matrix $\hat{\xi}_{nn'}$ is computed using Eq. (32).
- "Spectral Mapping": If the spectral mapping method is chosen, the following steps are performed:

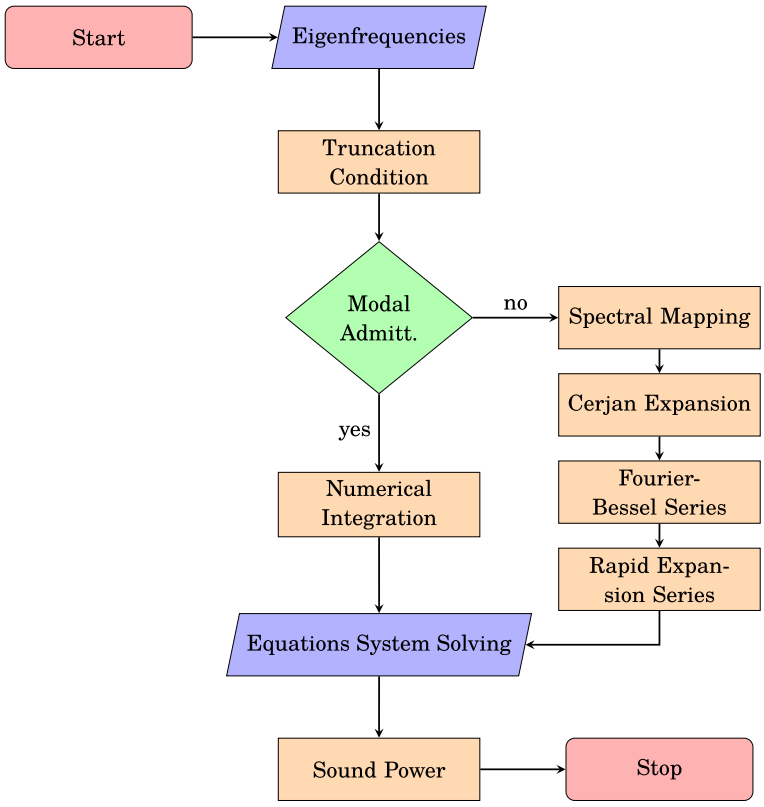


**Fig. E.13.** The TAFM numerical calculations scheme.

  - "Cerjan Expansion": The modal coefficients in Eqs. (61b) and (62c) are calculated. The truncation conditions for these expansions were discussed earlier by Rdzanek [50] (cf. the text after Eq. (38)), where it was empirically shown that sufficient accuracy is achieved for $\ell = 0, \ldots, L-1$, with $L = \mathrm{Round}(3m + 1.7\nu + 3)$. Appropriate bounds for $m$ and $\nu$ must first be determined. These bounds are obtained from the characteristic equation following Eq. (56) for the eigenvalues $\gamma_\nu^{|m|}$. Once these eigenvalues are found (as zeros of the characteristic equation), the values of $m$ and $\nu$ corresponding to all $\gamma_\nu^{|m|} \leqslant 2\pi f/c$ are collected. These values are then increased by the factor $\Delta N$ (see the discussion of the MNI after Fig. 3).
  - "Fourier-Bessel Series": The modal coefficients in Eqs. (60) and (62b) are computed, followed by the coefficients in Eq. (59).
  - "Rapid Expansion Series': The modal admittance coefficients in Eq. (56) are tabulated for each frequency. This requires first tabulating the coefficients in Eq. (57) based on Eqs. (65)–(70b).
- "Equations System Solving": The system of equations in Eq. (35) is solved numerically for each excitation frequency, yielding the modal coefficients $c_n$ used in the modal expansions in Eqs. (17a) and (17b).
- "Sound Power": Once the coefficients $c_n$ are determined, all vibroacoustic quantities can be calculated, including the acoustic power in Eq. (42), the acoustic pressure amplitude on the plate in Eq. (40), the acoustic pressure amplitude outside the plate in Eq. (24) with the Green function derivative in Eq. (B.2), and the normal component of vibration velocity on the plate from Eq. (17a). This concludes the procedure.

## References

[1] F. Leppington, E. Broadbent, K. Heron, The acoustic radiation efficiency of rectangular panels, Proc. R. Soc. London A 382 (1982) 245–271. https://doi.org/10.1098/rspa.1982.0100
[2] A. Berry, J. Guyader, J. Nicolas, A general formulation for the sound radiation from rectangular, baffled plates with arbitrary boundary conditions, J. Acoust. Soc. Am. 86 (6) (1990) 2792–2802.
[3] N. Atalla, J. Nicolas, C. Gauthier, Acoustic radiation of an unbaffled vibrating plate with general elastic boundary conditions, J. Acoust. Soc. Am. 99 (3) (1996) 1484–1494.
[4] C.-C. Sung, J. Jan, The response of and sound power radiated by a clamped rectangular plate, J. Sound Vib. 207 (3) (1997) 301–317.
[5] B. Laulagnet, Sound radiation by a simply supported unbaffled plate, J. Acoust. Soc. Am. 103 (5) (1998) 2451–2462.
[6] W. Li, H. Gibeling, Determination of the mutual radiation resistances of a rectangular plate and their impact on the radiated sound power, J. Sound Vib. 229 (5) (2000) 1213–1233.
[7] W. Li, An analytical solution for the self- and mutual radiation resistances of a rectangular plate, J. Sound Vib. 245 (1) (2001) 1–16. https://doi.org/10.1006/jsvi.2000.3552
[8] N. Hashimoto, Measurement of sound radiation efficiency by the discrete calculation methods, Appl. Acoust. 62 (2001) 429–446. https://doi.org/10.1016/S0003-682X(00)00025-6

[9] J. Arenas, M. Crocker, Sound radiation efficiency of a baffled rectangular plate excited by harmonic point forces using its surface resistance matrix, Int. J. Acoust. Vibr. 7 (4) (2002) 217–229.
[10] W. Zawieska, W. Rdzanek, Low frequency approximation of mutual modal radiation efficiency of a vibrating rectangular plate, Arch. Acoust. 31 (4S) (2006) 123–130. http://acoustics.ippt.pan.pl/index.php/aa/article/view/1332/1152.
[11] W. Zawieska, W. Rdzanek, W. Rdzanek, Z. Engel, Low frequency estimation for the sound radiation efficiency of some simply supported flat plates, Acta Acust. United Acust. 93 (3) (2007) 353–363. http://www.ingentaconnect.com/content/dav/aaua/2007/00000093/00000003/art00004.
[12] M.N. Currey, K.A. Cunefare, The radiation modes of baffled finite plates, J. Acoust. Soc. Am. 98 (3) (1995) 1570–1580. https://doi.org/10.1121/1.413423
[13] D. Zou, M.J. Crocker, Sound power radiated from rectangular plates, Arch. Acoust. 34 (1) (2009) 25–39. https://acoustics.ippt.pan.pl/index.php/aa/article/view/564.
[14] A. Putra, D. Thompson, Sound radiation from rectangular baffled and unbaffled plates, Appl. Acoust. 71 (12) (2010) 1113–1125. https://doi.org/10.1016/j.apacoust.2010.06.009
[15] G. Warburton, The vibration of rectangular plates, Proc. Inst. Mech. Eng. 168 (1) (1954) 371–384. https://doi.org/10.1243/PIME_PROC_1954_168_040_02
[16] K. Kolber, A. Snakowska, M. Kozupa, The effect of plate discretization on accuracy of the sound radiation efficiency measurements, Arch. Acoust. 39 (4) (2014) 511–518. https://doi.org/10.2478/aoa-2014-0055
[17] T. Mellow, L. Kärkkäinen, Expansions for the radiation impedance of a rectangular piston in an infinite baffle, J. Acoust. Soc. Am. 140 (4) (2016) 2867–2875. https://doi.org/10.1121/1.4964632
[18] S. Hasheminejad, H. Keshavarzpour, Active sound radiation control of a thick piezolaminated smart rectangular plate, J. Sound Vib. 332 (20) (2013) 4798–4816. https://doi.org/10.1016/j.jsv.2013.04.028
[19] S. Hasheminejad, S. Parvasi, A. Fadavi-Ardakani, Vibroacoustic analysis and response suppression of a rectangular sandwich electrorheological panel, Int. J. Acoust. Vib. 21 (1) (2016) 81–92. https://doi.org/10.20855/ijav.2016.21.1398
[20] M. Pawelczyk, S. Wrona, Noise-Controlling Casings, 1st Edition, CRC PRESS, New York, New York, 2022. 264 pages.
[21] H. Dikshit, V.R. Sonti, Sound transmission of an obliquely incident plane wave through an unbaffled plate, J. Acoust. Soc. Am. 158 (2) (2025) 1177–1188. https://doi.org/10.1121/10.0038970
[22] H. Dikshit, A.A. Mana, V.R. Sonti, A closed form expression for the resonance frequencies of an unbaffled simply-supported rectangular water-loaded plate, Wave Motion 134 (2025). https://doi.org/10.1016/j.wavemoti.2025.103499
[23] Y. Xing, B. Liu, New exact solutions for free vibrations of rectangular thin plates by symplectic dual method, Acta Mech. Sinica/Lixue Xuebao 25 (2) (2009) 265–270. https://doi.org/10.1007/s10409-008-0208-4
[24] J. Cornacchio, R. Soni, On a relation between two-dimensional Fourier integrals and series of Hankel transforms, J. Res. Natl. Bureau Standards-B Math. Math. Phys. 69 (3) (1965) 173–174. https://doi.org/10.6028/jres.069b.020
[25] N. Baddour, Operational and convolution properties of two-dimensional Fourier transforms in polar coordinates, J. Opt. Soc. Am. A Opt. Image Sci. Vision 26 (8) (2009) 1767–1777. https://doi.org/10.1364/JOSAA.26.001767
[26] W. Rdzanek, K. Szemela, Sound radiation by a vibrating annular plate using radial polynomials and spectral mapping, J. Acoust. Soc. Am. 146 (4) (2019) 2682–2691. https://doi.org/10.1121/1.5130193
[27] A. Pierce, Acoustics, An Introduction to Its Physical Principles and Applications, Acoustical Society of America through American Institute of Physics, New York, New York, 1994. 678 pages.
[28] D. Blackstock, in: Fundamentals of Physical Acoustics, John Wiley and Sons, 2000. 541 pages.
[29] L. Meirovitch, Analytical Methods in Vibrations, New York, MacMillan, 1967. 555 pages.
[30] S. Rao, Vibrations of Continuous Systems, Wiley, New Jersey, New Jersey, 2007. 720 pages.
[31] H. Levine, F. Leppington, A note on the acoustic power output of a circular plate, J. Sound Vib. 121 (2) (1988) 269–275. https://doi.org/10.1016/S0022-460X(88)80029-4
[32] F. Fahy, P. Gardonio, Sound and Structural Vibration. Radiation, Transmission and Response, 2nd Edition, Academic Press Elsevier, 2007. 633 pages.
[33] E. Williams, Fourier Acoustics. Sound Radiation and Nearfield Acoustical Holography, London, Academic Press, 1999. 306 pages.
[34] M. Amabili, G. Frosali, M. Kwak, Free vibrations of annular plates coupled with fluids, J. Sound Vib. 191 (5) (1996) 825–846. https://doi.org/10.1006/jsvi.1996.0158
[35] W. Rdzanek, J. Wiciak, M. Pawelczyk, Analysis of sound radiation from a vibrating elastically supported annular plate using compatibility layer and radial polynomials, J. Sound Vib. 519 (2022) 1–24. https://doi.org/10.1016/j.jsv.2021.116593
[36] D. Duffy, Green's Functions with Applications, Studies in Advanced Mathematics, Chapman & Hall/CRC, New York, New York, 2001. 651 pages.
[37] G. Lovat, S. Celozzi, Rapidly convergent series and closed-form expressions for a class of integrals involving products of spherical Bessel functions, J. Comput. Appl. Math. 445 (1–19) (2024). https://doi.org/10.1016/j.cam.2024.115802
[38] Handbook of Mathematical Functions with Formulas, Graphs, and Mathematical Tables, Technical Report, U. S. Department of Commerce, National Bureau of Standards, 1972. 1046 pages.
[39] P. Morse, K. Ingard, T. Acoustics, Princeton University Press, New Jersey, New Jersey, 1968. 927 pages.
[40] W. Rdzanek, W. Rdzanek, K. Szemela, Asymptotic approximation of the modal acoustic impedance of a circular membrane, J. Comput. Acoust. 18 (4) (2010) 335–362. https://doi.org/10.1142/S0218396X1000422X
[41] R. Aarts, A. Janssen, Sound radiation quantities arising from a resilient circular radiator, J. Acoust. Soc. Am. 126 (4) (2009) 1776–1787. https://doi.org/10.1121/1.3206580
[42] The mpmath development team, mpmath: a Python library for arbitrary-precision floating-point arithmetic, 2023. Version 1.3.0), http://mpmath.org/.
[43] G. Squicciarini, D. Thompson, R. Corradi, The effect of different combinations of boundary conditions on the average radiation efficiency of rectangular plates, J. Sound Vib. 333 (17) (2014) 3931–3948. https://doi.org/10.1016/j.jsv.2014.04.022
[44] A. Leissa, SP-160 of NASA Technical Reports, National Aeronautics and Space Administration, in: Vibration of Plates, Washington D.C., 1969. 353 pages, http://ntrs.nasa.gov/search.jsp?R=19700009156.
[45] L. Bao, S. Yuchen, W. Deshi, The baffle influence on sound radiation characteristics of a plate, MATEC Web Conf 128 (2017) 05006. https://doi.org/10.1051/matecconf/201712805006
[46] N.M. Mohammed, S.C. Creagh, G. Tanner, Acoustic radiation from random waves on plates, J. Phys. A Math. Theor. 55 (39) (2022) 394004. https://doi.org/10.1088/1751-8121/ac8c08
[47] F. Olver, D. Lozier, R, NIST Handbook of Mathematical Functions, Cambridge University Press, 2010. 951 pages.
[48] J. Wimp, Polynomial expansions of Bessel functions and some associated functions, Math. Comput. 16 (80) (1962) 446–457. https://doi.org/10.1090/S0025-5718-1962-0148956-3
[49] I. Gradshteyn, I. Ryzhik, Table of Integrals, Series, and Products, 7th Edition, New York, Academic Press, 2007. 1171 pages.
[50] W. Rdzanek, The acoustic power of a vibrating clamped circular plate revisited in the wide low frequency range using expansion into the radial polynomials, J. Acoust. Soc. Am. 139 (6) (2016) 3199–3213. https://doi.org/10.1121/1.4954265